P-62

NASA CR-189140

PLASMA CONTACTOR RESEARCH - 1991

Prepared for

LEWIS RESEARCH CENTER

NATIONAL AERONAUTICS AND SPACE ADMINISTRATION

Grant NAG 3-776

Annual Report

April 1992

Approved by

Paul J. Wilbur
Department of Mechanical Engineering
Colorado State University
Fort Collins, Colorado 80523

NASA
National Aeronautics and Space Administration

Report Documentation Page

1. Report No.	2. Government Accession No.	3. Recipient's Catalog No.
CR 189140		

4. Title and Subtitle
Plasma Contactor Research - 1991

5. Report Date
April 1992

6. Performing Organization Code

7. Author(s)
Brett Buchholtz
John D. Williams
Paul J. Wilbur

8. Performing Organization Report No.

10. Work Unit No.

9. Performing Organization Name and Address
Department of Mechanical Engineering
Colorado State University
Fort Collins, CO 80523

11. Contract or Grant No.
NAG 3-776

13. Type of Report and Period Covered
Annual:
Jan. 1, 1991 - Jan. 1, 1992

12. Sponsoring Agency Name and Address
National Aeronautics and Space Administration
Washington, D.C. 20546

14. Sponsoring Agency Code

15. Supplementary Notes
Grant Monitor- Joel T. Galofaro
NASA Lewis Research Center
Cleveland, Oh 44135

16. Abstract

A report describing the operating principles of hollow-cathode-based plasma contactors emitting or collecting electrons from an ambient plasma is summarized. Preliminary experiments conducted to determine the noise generated by these plasma contactors in the emission-current return line and in the plasma near it are described. These noise data are measured as current fluctuations in the return line and to a Langmuir probe and then analyzed using a fast-Fourier-transform technique. The spectral compositions of the data are characterized using power-spectral-density plots which are examined to identify possible noise source(s) and production mechanism(s). The precautions taken in the construction and calibration of the instrumentation to assure adequate frequency response are described. Experimental results show that line-current noise levels are typically 2% of the electron current being emitted or collected. However, noise levels increase to as much as 20% of the electron current at a few electron-collection operating conditions. The frequencies associated with most of the noise were harmonics of the 60 Hz input to system power supplies. Plasma noise had characteristics similar in magnitude and frequency to those for the return-line noise, but they contained additional features at frequencies considered to be related to ion-acoustic instabilities. Also discussed is a new probe positioning system built to facilitate future plasma-contactor research.

17. Key Words (Suggested by Author(s))	18. Distribution Statement
Plasma Contactor Hollow Cathode Noise	Unclassified - Unlimited

19. Security Classif. (of this report)	20. Security Classif. (of this page)	21. No of pages	22. Price*
Unclassified	Unclassified	67	

NASA FORM 1626 OCT 86

*For sale by the National Technical Information Service, Springfield, Virginia 22161

TABLE OF CONTENTS

LIST OF FIGURES

AN EXPERIMENTAL INVESTIGATION OF HOLLOW-CATHODE-BASED PLASMA CONTACTORS

John D. Williams

Summary

A major research effort designed to identify the steady-state operating characteristics of hollow-cathode-based plasma contactors was completed during the period covered by this report. The complete results of this work and the conclusions drawn from it are given in Ref. [1] and they will be repeated here only in summary. Reference [1] presents experimental results which describe the operation and the plasma environment downstream of a hollow-cathode-based plasma contactor collecting electrons from or emitting them to an ambient, low-density, Maxwellian plasma. A one-dimensional, phenomenological model of the near-field electron collection process, which was formulated from experimental observations, is presented. The model identifies three distinct plasma regions, namely, a plasma cloud adjacent to the contactor, an ambient plasma from which electrons are collected, and a double-layer region that develops between these two plasma regions. Results of electron emission experiments are also presented. An important observation is made on the basis of retarding potential analyzer (RPA) measurements which show that high energy ions generally stream from a contactor along with the electrons being emitted. A mechanism for this phenomenon is presented. It involves a high rate of ionization induced between electrons and atoms flowing together from the hollow-cathode

orifice. It is suggested that this can result in the development of a region of high positive space charge and, therefore, high positive potential. Langmuir and RPA probe data suggest that both electrons and ions expand spherically downstream from this potential-hill region. In addition to experimental observations, a one-dimensional model which describes the electron-emission process and predicts the phenomena just described is presented and shown to agree qualitatively with measured results.

NOISE ASSOCIATED WITH HOLLOW-CATHODE-BASED PLASMA CONTACTOR OPERATION

Brett Buchholtz

Introduction

Hollow-cathode plasma contactors have been proposed for use on spacecraft because of their ability to emit electrons to or collect them from an adjacent space plasma and thereby hold spacecraft potentials close to the potential of that plasma. Results obtained in the laboratory [1,2,3] and numerical analyses [4] suggest that they should be able to conduct either the modest currents associated with natural charging events [5] or the more substantial ones which are expected when devices such as the electrodynamic tether are operated [6]. In order to minimize interference with communications equipment, on-board electronics and instrumentation, it is important that the plasma contacting process induce minimal electromagnetic noise whether it be radiated into space or transmitted directly into the spacecraft-ground network. If noise is generated, it is important that its frequency and amplitude characteristics be known so proper filtering precautions can be introduced. Further, the effects of changes in contactor operating conditions on the characteristics of the induced noise should be known and understood.

Although in-space experiments will ultimately be required to demonstrate the noise characteristics of plasma contactors in that environment, ground-based experiments provide useful insight into the magnitudes, frequencies, and causes of electrical noise associated with the plasma-contacting process. Results from the less costly ground-based tests can serve as a guide to hollow-cathode-plasma-contactor

design and the eventual conduct of space experiments. This report describes an initial ground-based investigation of the noise produced by a plasma contactor that can emit electrons to or collect them from a plasma source (the simulator) that produces a diffuse ambient plasma in a vacuum chamber housing the contactor.

In general, noise appears as "hash" or random fluctuations about mean values of variables such as currents or voltages. The noise produced by a plasma contactor, for example, can be expressed in terms of current fluctuations about the mean electron current being emitted or collected. Contactor noise may also be reflected in potential and/or density fluctuations in the plasma surrounding the contactor. This noise can be detected by a Langmuir probe in the form of fluctuations in the current being drawn to the probe. Information can be extracted from fluctuating signals like the two just described by transforming the temporal fluctuation data into the frequency domain. An examination of the transformed data can reveal dominant frequencies in the power spectrum (a plot of power within a narrow bandwidth against frequency). From this specific information it should be possible to understand the mechanisms that induce the noise and to design and construct filters that will reduce or eliminate its undesirable effects.

This report will focus on 1) the construction of the instrumentation used to make electrical-noise measurements associated with hollow-cathode-based plasma contactor operation and 2) preliminary experimental results and first order interpretations of the noise measured under various plasma contactor operating conditions. The instrumentation includes Langmuir probes, filters and a digital oscilloscope used to sense and record the signals. Calibration procedures that were designed to demonstrate adequate frequency response of the system up to the

frequency limit of the oscilloscope (100 kHz) will be shown. Experimental results that illustrate the general nature of the noise produced under quiet and noisy contactor operating modes will be presented.

Apparatus and Procedures

Noise data were collected while a hollow-cathode plasma contactor was exchanging current with an ambient plasma in the 5.3 m long by 1.2 m diam. cylindrical vacuum tank shown schematically in Fig. 1. The ambient plasma was generated principally by the simulator shown near the center of the tank. The plasma contactor was mounted at one end of the vacuum tank and it actually emitted electrons to or collected them from this simulator via the ambient plasma. Plasma properties were measured using spherical Langmuir and emissive probes attached to a probe support rod which positioned them radially and axially in the region between the contactor and simulator (Fig. 1).

The hollow-cathode plasma contactor used for all of the noise experiments is similar to one used in previous contactor performance studies [1,2,3]. This contactor, which is shown schematically in Fig. 2a, consisted of a 0.6 cm diameter tantalum hollow-cathode tube capped by a thoriated-tungsten plate with a 1.0 mm diameter orifice. A tantalum-foil insert located within the cathode was coated with a low work-function materials ($BaCO_3$ and $SrCO_3$) which served to provide electrons at modest temperatures. During operation, a discharge was maintained between the cathode and an anode located $\sim$4 mm downstream. The anode is a 1.3 cm I.D by 12 cm O.D. stainless steel plate with a 3 mm I.D. by 5 mm O.D. tantalum loop at its center (Fig. 2a). The loop is made of refractory metal so it will withstand melting at the temperatures induced in region of the anode nearest the cathode under some

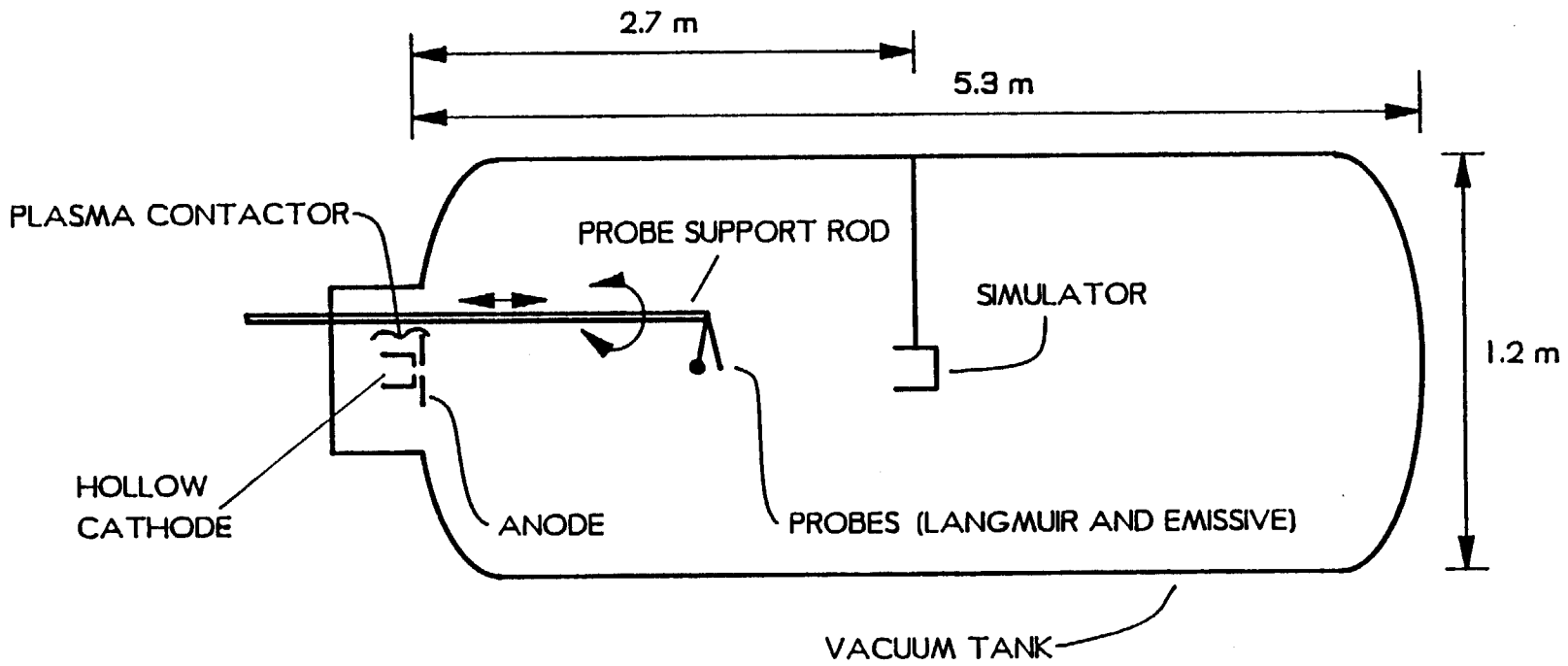

Fig. 1 Mechanical Diagram Schematic

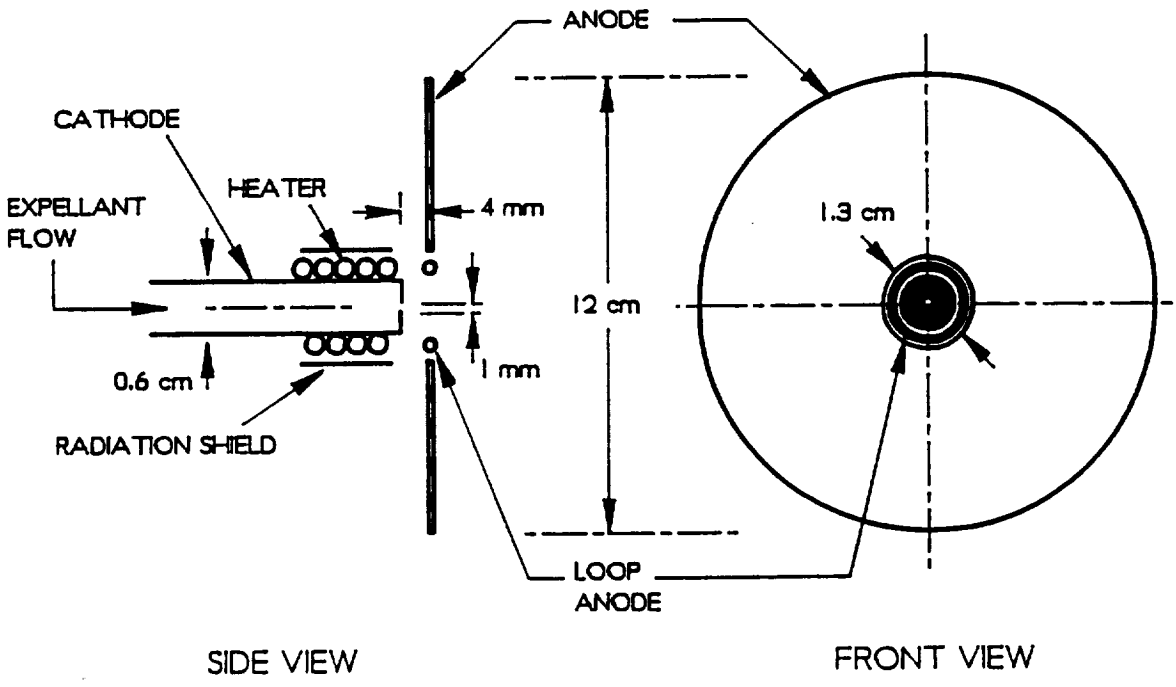

a) Hollow Cathode Plasma Contactor Schematic

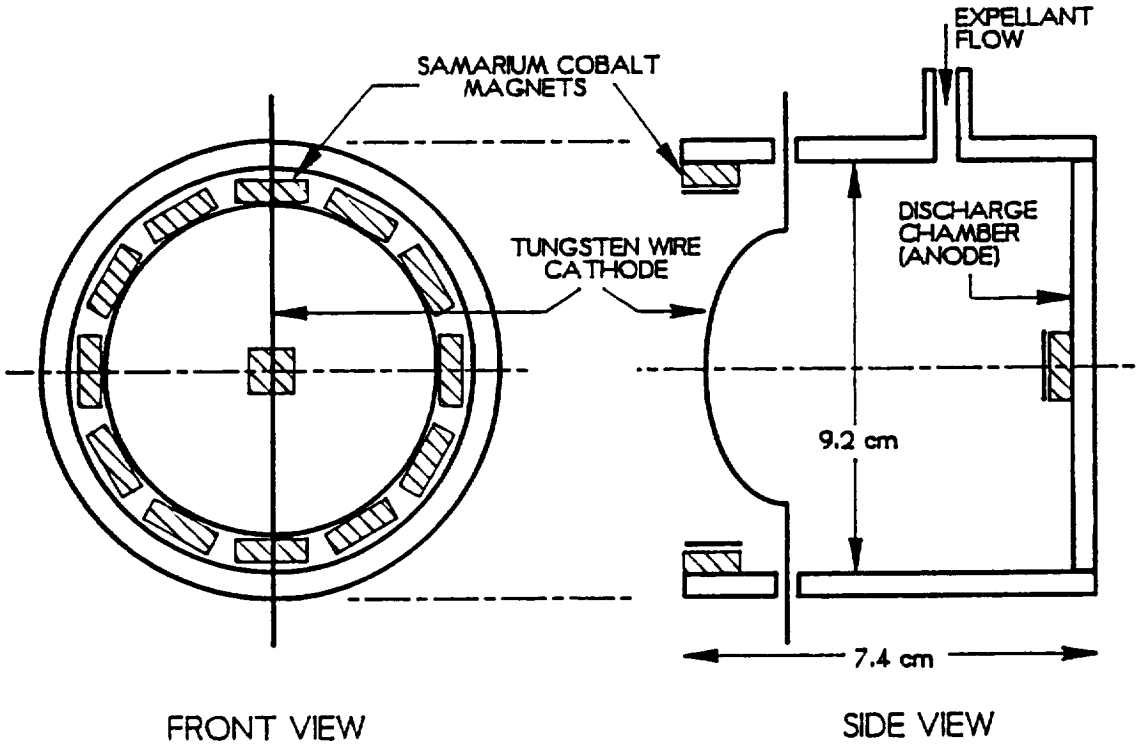

b) Simulator Schematic

Fig. 2 Plasma Contactor and Simulator Schematics

higher discharge-current operating conditions.

The simulator used for the experiments is shown schematically in Fig. 2b. It consists of a mild-steel, cylindrical discharge chamber with an inner diameter of 9.2 cm and a length of 7.4 cm which houses a cathode and some magnets. The cathode, which emits electrons thermionically, is fabricated from 0.25 mm diameter tungsten wire and the magnets are made of samarium-cobalt. The field induced by the magnets impedes the flow of electrons from the cathode to the anode (Fig. 2b) until they have had many opportunities to have inelastic collisions with atoms supplied into the chamber. These collisions result in the production of ions needed to sustain the ambient plasma. Both the contactor and simulator used xenon gas as expellants.

The plasma contactor and simulator were connected in the electrical configuration shown schematically in Fig. 3. With the switches depicted in the figure toggled to their proper place, the plasma contactor could either emit electrons (EE) to or collect electrons (EC) from the simulator. Noise measurements were made in the emission current return line by recording current fluctuations in the form of voltage fluctuations across the 1 Ω resistors shown in Fig. 3 (Resistor A for electron emission and Resistor B for electron collection). These current fluctuations will be designated the "line noise" in the text that follows. Additional noise measurements made in the plasma downstream of the contactor were sensed as current fluctuations to the Langmuir probe when it was biased at local plasma potential. The fluctuations will be designated as the "plasma noise". For both line and plasma noise measurements, care was exercised to ensure that 1) the overall response of the instrumentation was adequate to provide accurate frequency detection within the range of frequencies being investigated and 2) the data were properly filtered to prevent the appearance of

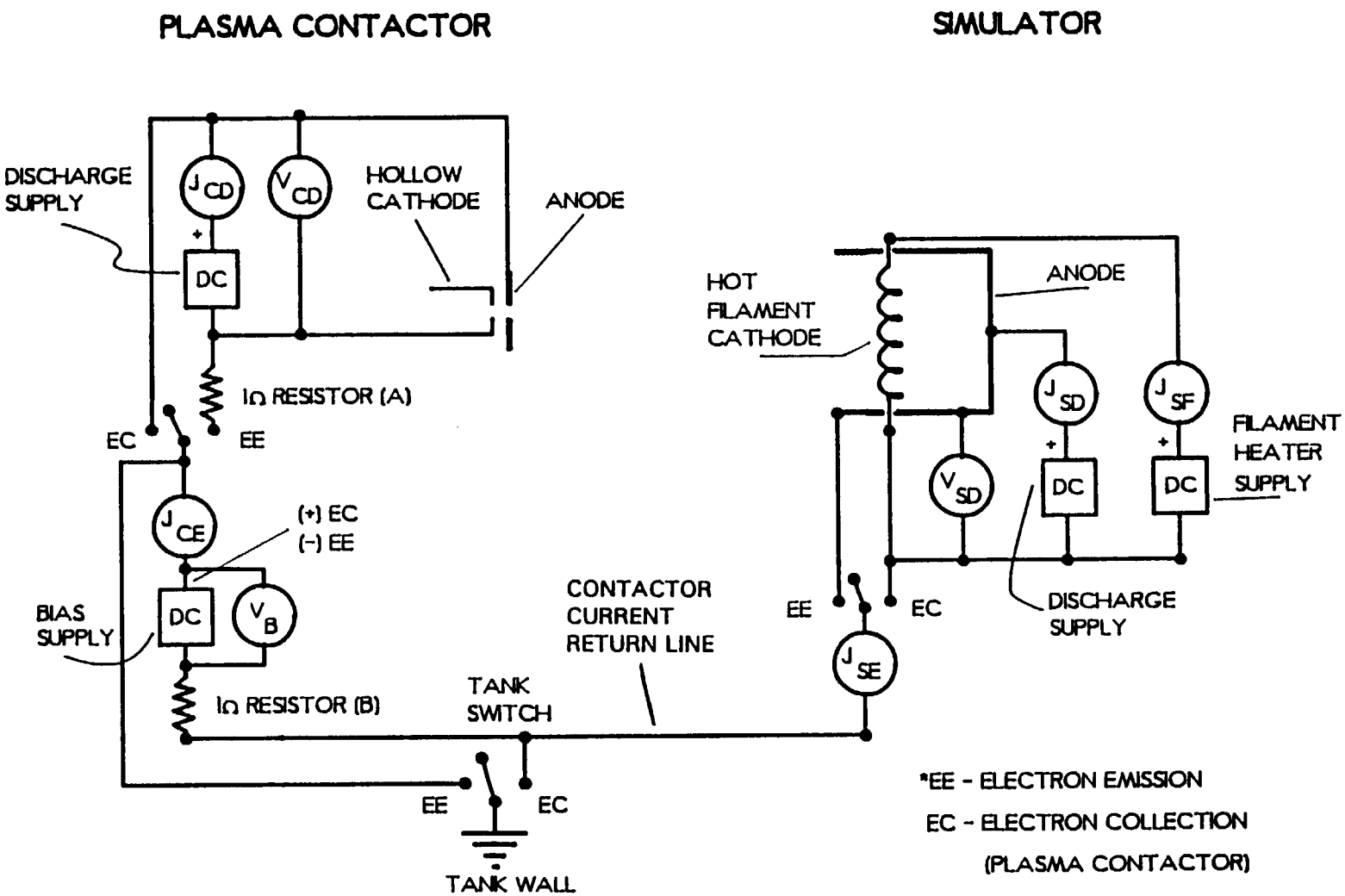

Fig. 3 Electrical Schematic

erroneous, aliased data in fast Fourier transform output and

The fast Fourier transform (FFT) technique [7,8] was used to transform discrete, fluctuating-voltage noise data which had been sensed and recorded, into the frequency domain. A FFT computer code similar to that used for data analysis in this report can be found in Reference [7]. Appendix A provides an explanation of the important steps used to acquire, transform (into the frequency domain), and interpret noise data using the FFT. Data in the frequency domain are often presented in a standard power-spectral-density (PSD) format where PSD is plotted against frequency. The PSD is defined as the mean-squared amplitude of a signal at a given frequency divided by the bandwidth associated with the measurement [9]. The resulting plots can be integrated over a prescribed frequency range to obtain a mean-square value of the amplitude for that frequency range (see Appendix A).

Instrumentation Calibration

In order to 1) characterize the frequency response of the instrumentation used to sense, transmit, and record noise data and 2) evaluate the software used convert the data into power-spectral-density plots, signals of known frequency and amplitude were inputed to two different portions of the system. First, the suitability of the 20 dB/decade (1-pole) filter built into the oscilloscope was tested in conjunction with the fast Fourier transform (FFT) computer program. The physical arrangement of the test is shown in Fig. 4a. It involved transmission of a 3.5 V amplitude sine-wave signal from a wave generator into the filter first at a frequency of 100 Hz and then at 1 kHz, 2 kHz, 5 kHz, and 10 kHz. The bandpass frequency range of the filter was set from 10 to 1000 Hz and the sampling rate of the oscilloscope was set at 10.2 kHz (10,200 data points/sec.). This sampling rate, in turn, determines the greatest

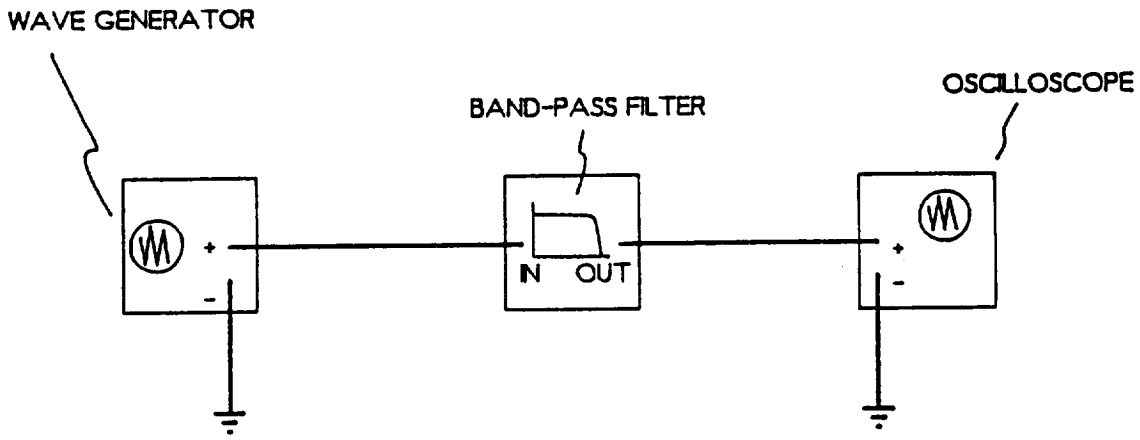

a) Testing of the Filter

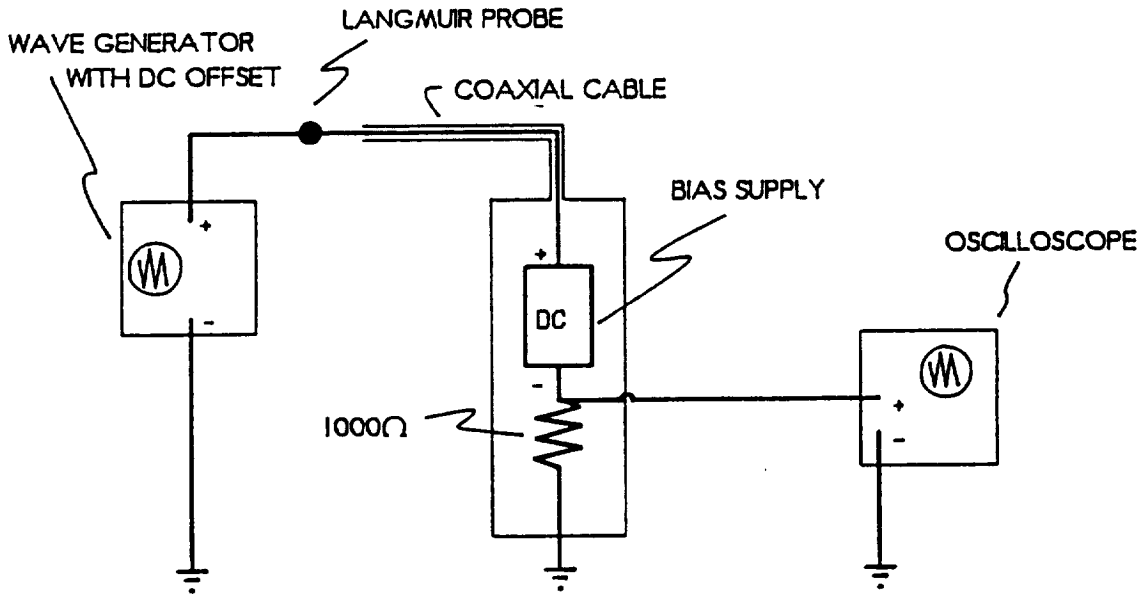

b) Testing of the Frequency Response

Fig. 4 Schematics for Instrumentation Tests

frequency that can be detected (the cutoff frequency) without violating the Nyquist criterion [7,8,9]. This criterion requires that at least two data points be collected during the period of the wave at the cutoff frequency. Hence, at a 10.2 kHz sampling rate, the cutoff frequency is ~5000 Hz and signals having higher frequencies must be filtered out to prevent the problem of "aliasing" discussed in Appendix A. Therefore, the 10 kHz signal, which is being introduced in this test, is likely to be aliased when the discrete FFT analysis is performed unless the filter (with high frequency limit at 1000 Hz) attenuates it sufficiently.

The PSD data associated with the experiment were computed using the FFT computer program and they are plotted as PSD against frequency in Fig. 5 on a log-log scale. The results show all of the input signals, except the 10 kHz one at the proper frequencies. The PSD magnitudes for the 2 and 5 kHz signals are slightly attenuated as expected, and the 10 kHz signal, which has been aliased to ~700 Hz, has also been attenuated, but not enough to make it disappear in the white, background noise. These results suggest a better filter, with a sharper roll-off, is needed in order to eliminate the aliased signal(s).

A new, 4-pole Butterworth electronic filter with 80 dB/decade roll-off [10], which was expected to do a better job of removing the high-frequency, aliased signal, was designed, built and tested. To illustrate the difference in roll-off, both the old and new filters were calibrated by inputting a sine wave of known voltage amplitude (A_{in}) at a particular frequency while sensing and recording the output voltage amplitude (A_{out}). The calibrations were carried out at three different bandwidths (bandpass settings on the filters) and for input signals which covered the frequency range from 1 to 10^6 Hz. Output-to-input amplitude ratios are plotted as a function of

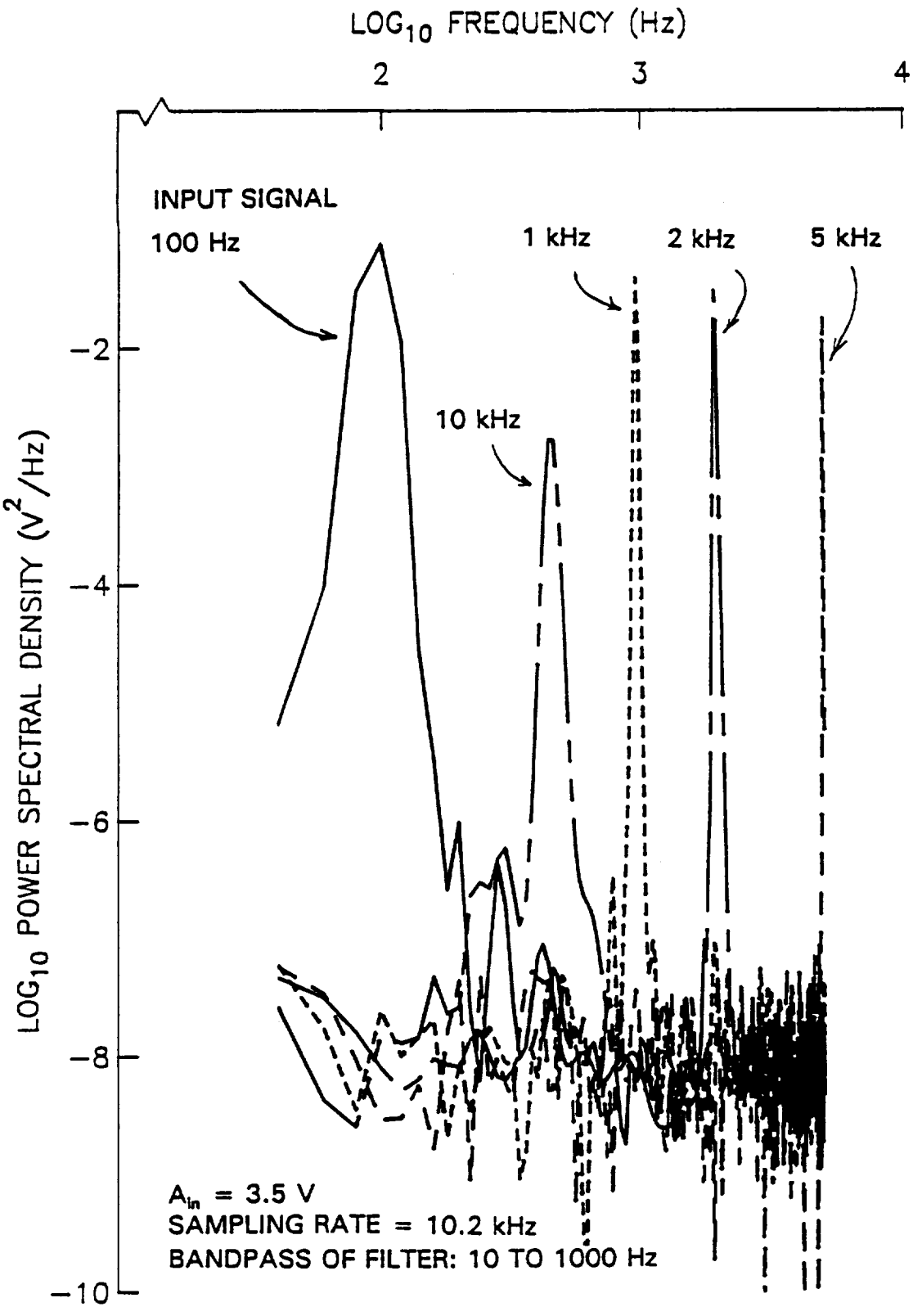

Fig. 5 Test Results From a 1-pole Filter

frequency on a log-log scale for the old and new filters in Fig. 6. In Fig. 6a it can be seen that the old filter is a 1-pole device and that it, therefore, attenuates the output signal at one decade of amplitude per decade of frequency above its cutoff frequency (i.e. at 6 dB/octave or 20 dB/decade). The new filter, on other hand, is a 4-pole unit (i.e. it attenuates at four decades of amplitude per decade of frequency, 24 dB/octave or 80 db/decade above the cutoff frequency) as shown by the data of Fig. 6b.

In order to illustrate the relative effectiveness of the filters, the new 4-pole filter was tested using the same configuration depicted in Fig. 4a and the procedure applied to the old filter; the resulting PSD are plotted in Fig. 7b. For comparison purposes, the results obtained using the old filter, Fig. 5, are re-plotted in Fig. 7a. Comparison of Figs. 7a and 7b shows the new, 4-pole filter attenuates the aliased 10 kHz signal much more effectively than the old, 1-pole one did and is, therefore, the preferred filter. It is also noted the upper frequency of the 4-pole filter was set at 1000 Hz, and therefore Fig. 7b shows the 2 and 5 kHz signals are significantly attenuated. In order to prevent this attenuation from interfering with contactor noise data, three bandpass ranges and sampling frequencies will be used when complete sets of data are collected. This will provide reasonable frequency resolution in a particular bandpass range while at the same time assuring that aliased signals have been attenuated adequately in the final output.

Another important concern for measuring noise associated with the plasma contactor was that the instrumentation should have a sufficiently high frequency response over the range of interest. Adequate frequency response is of greater concern for plasma noise than for line noise measurements because higher frequencies from beam instabilities are expected in the plasma downstream from the contactor. In

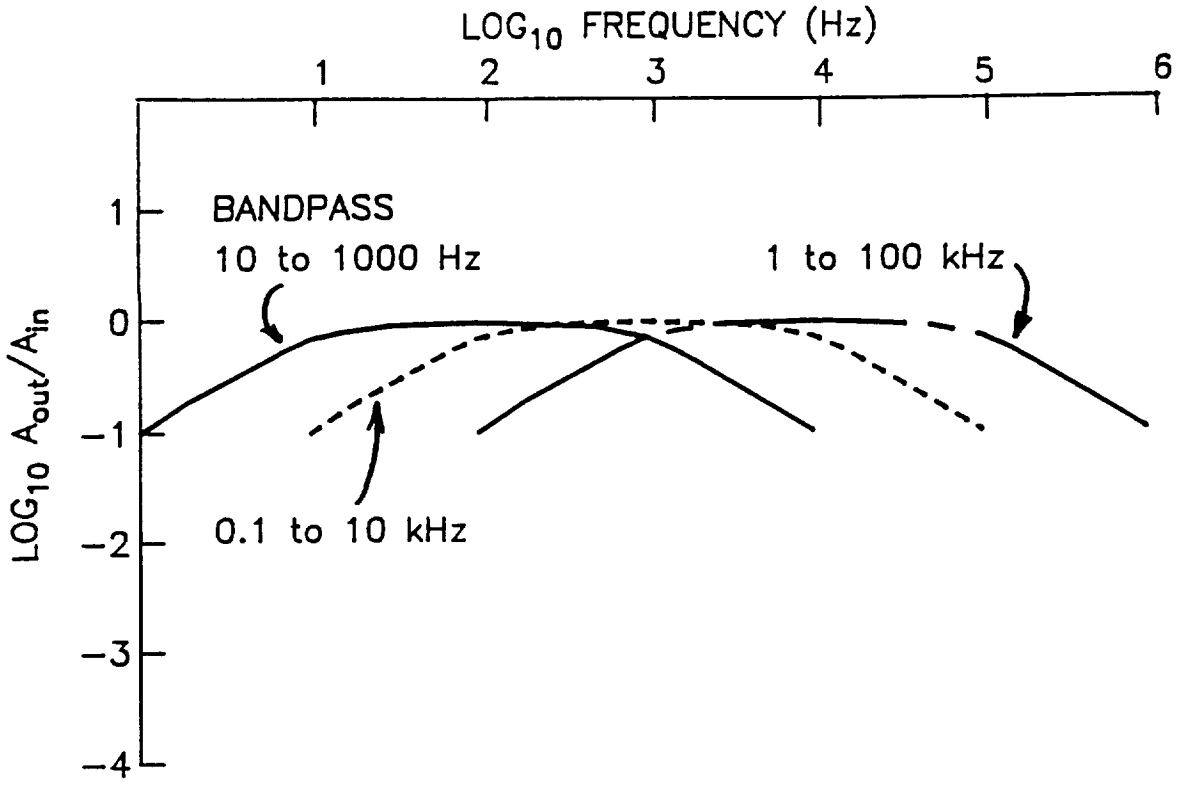

a) Frequency Responses of Old Filter (20 dB/Decade)

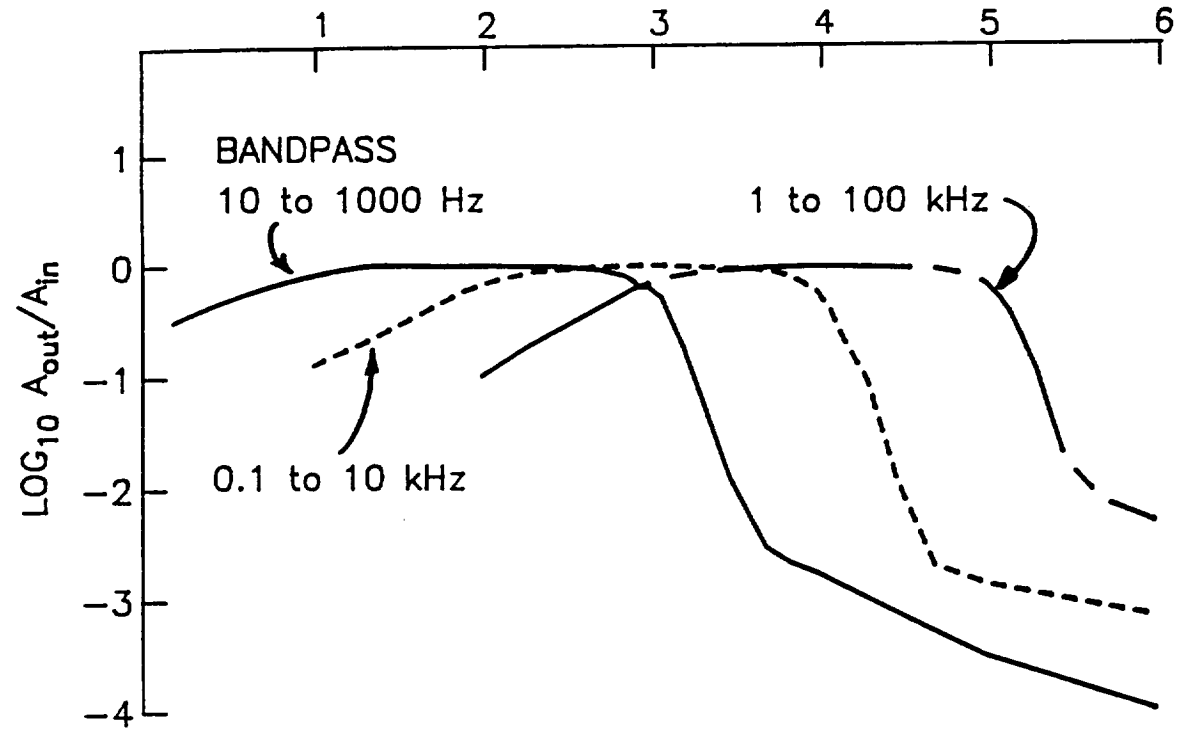

b) Frequency Responses of New Filter (80 dB/Decade)

Fig. 6 Test Results of the Filters

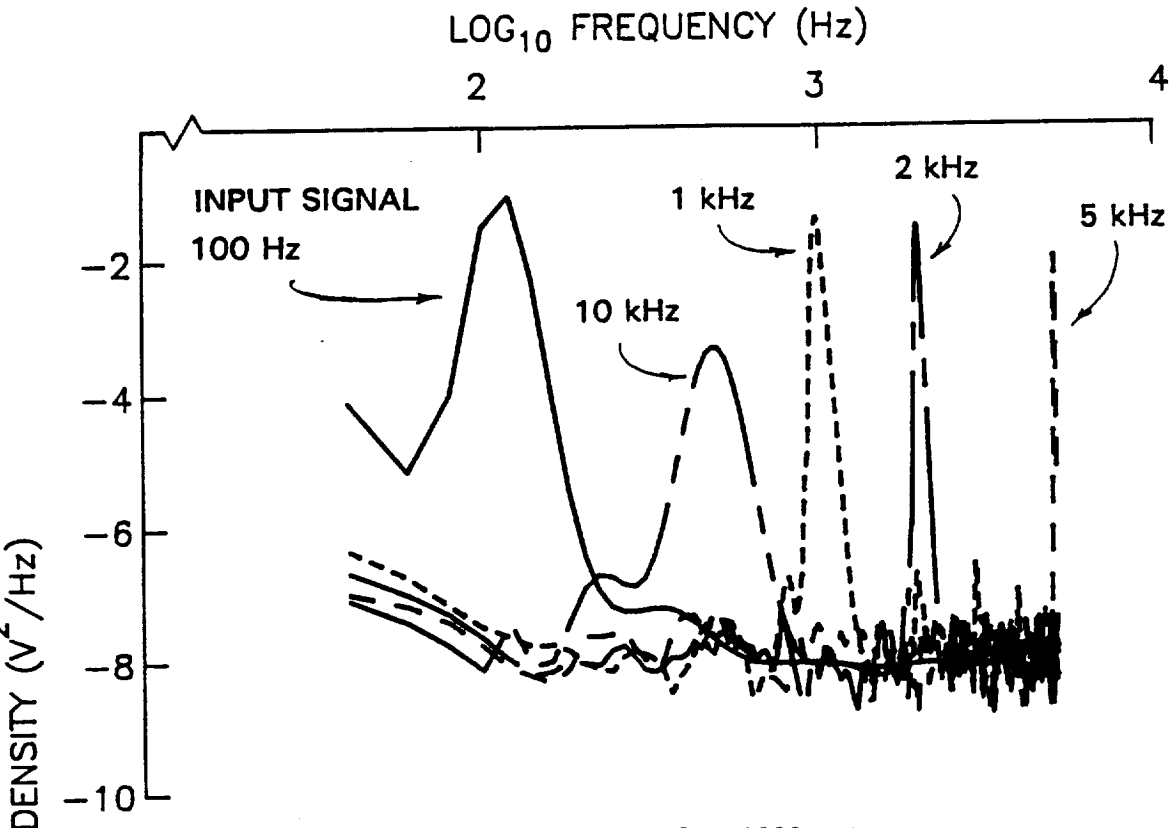

a) Using the 1-pole Filter (Bandpass 10 to 1000 Hz)

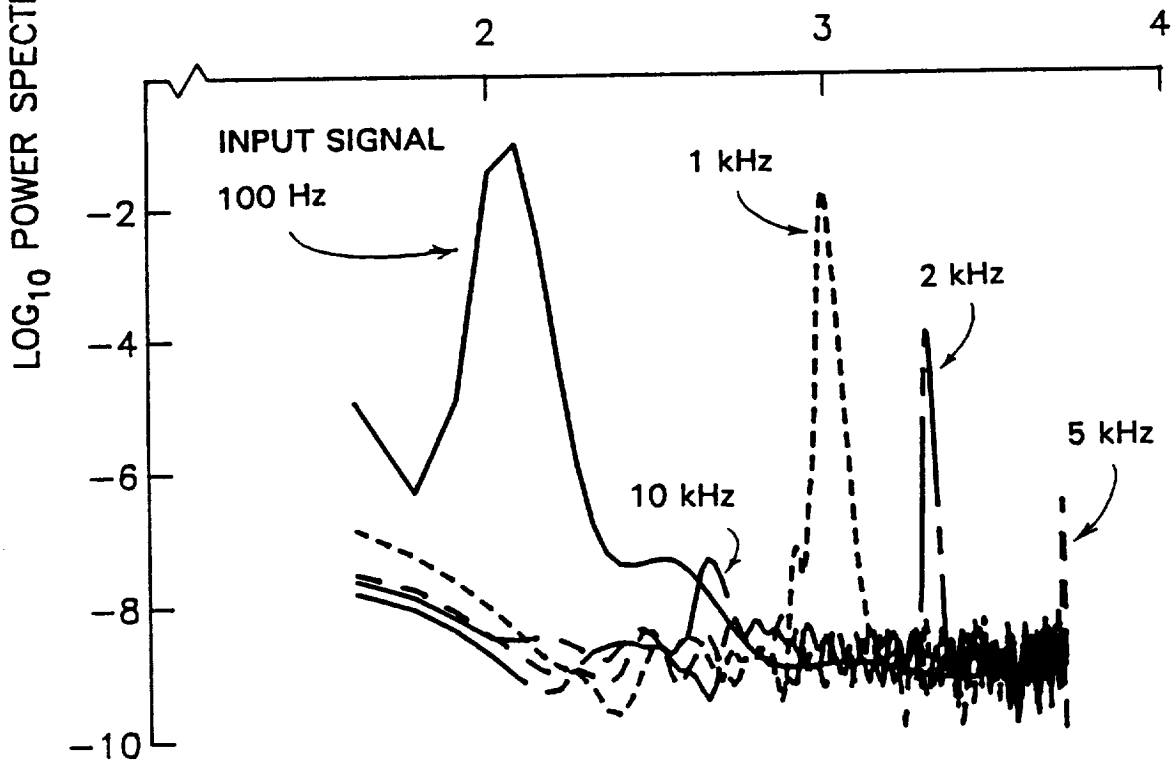

b) Using the 4-pole Filter (Bandpass 10 to 1000 Hz)

Fig. 7 Test Results of the Filters

order to detect these frequencies, plasma noise measurements were made by biasing a Langmuir probe to plasma potential and then recording probe-current fluctuations by sensing voltage fluctuations across a 1000 Ω shunt resistor in the line to the probe. The arrangement used to investigate the frequency response of this system is shown schematically in Fig. 4b. It consists of a wave generator connected to a biased-Langmuir-probe system (i.e. one biased positive as it would be when used to make measurements in a plasma). The wave generator had a DC-offset capability so its mean potential could be adjusted to match the bias voltage applied to the probe. The wave generator supplied a sinusoidal signal of prescribed frequency and voltage amplitude (A_{in}) between the Langmuir probe and ground. The output signal, A_{out}, was detected by the oscilloscope across the 1000 Ω resistor shown in Fig. 4b. In order to investigate the probe system frequency response, the wave amplitude (A_{in}), wave frequency, DC offset, and coaxial cable length were each varied.

The effect different wave amplitudes had on the frequency response was investigated by setting the probe bias voltage at 5 V and measuring A_{out} over the frequency range 10 Hz to 10 MHz at various input amplitudes. Typical results (for 4 and 8 V amplitudes) are given in Fig. 8 in the form of a plot of output-to-input amplitude ratio (A_{out}/A_{in}) against input frequency on a log-log scale. This figure shows that 1) the amplitude ratio is near unity (i.e. Log_{10} of the amplitude is near zero) up to 10^5 Hz and 2) the frequency response is the same at both input signal amplitudes. The effect different probe potentials had on the frequency response was studied in a similar fashion by holding A_{in} at 2 V, and changing the bias voltage from 0 to 5 to 10 V. Again amplitude ratios (A_{out}/A_{in}) were computed from the measured amplitudes over the same frequency range and the results are plotted in Fig. 9 on a

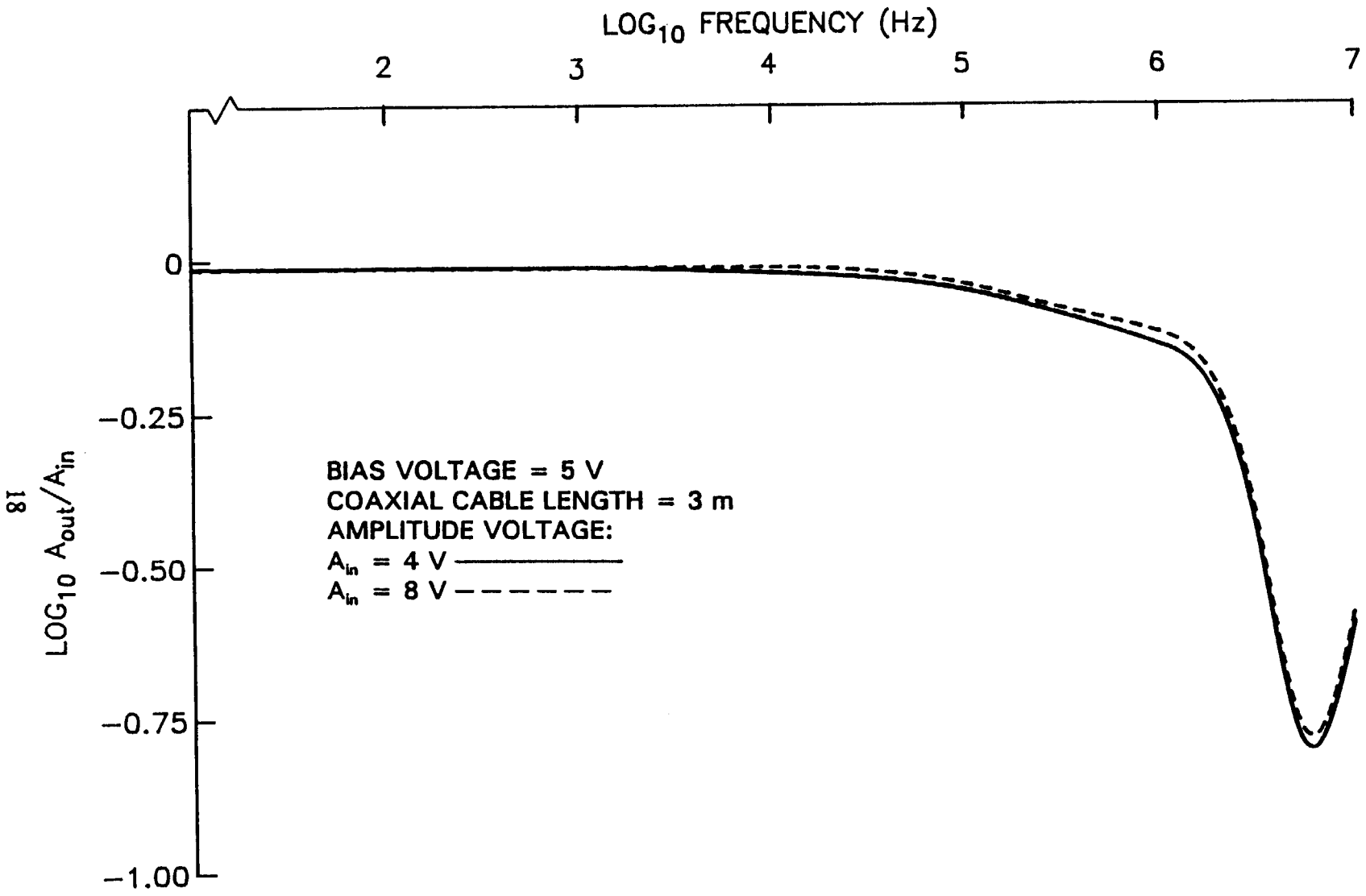

Fig. 8 Effect of A_{in} on Frequency Response

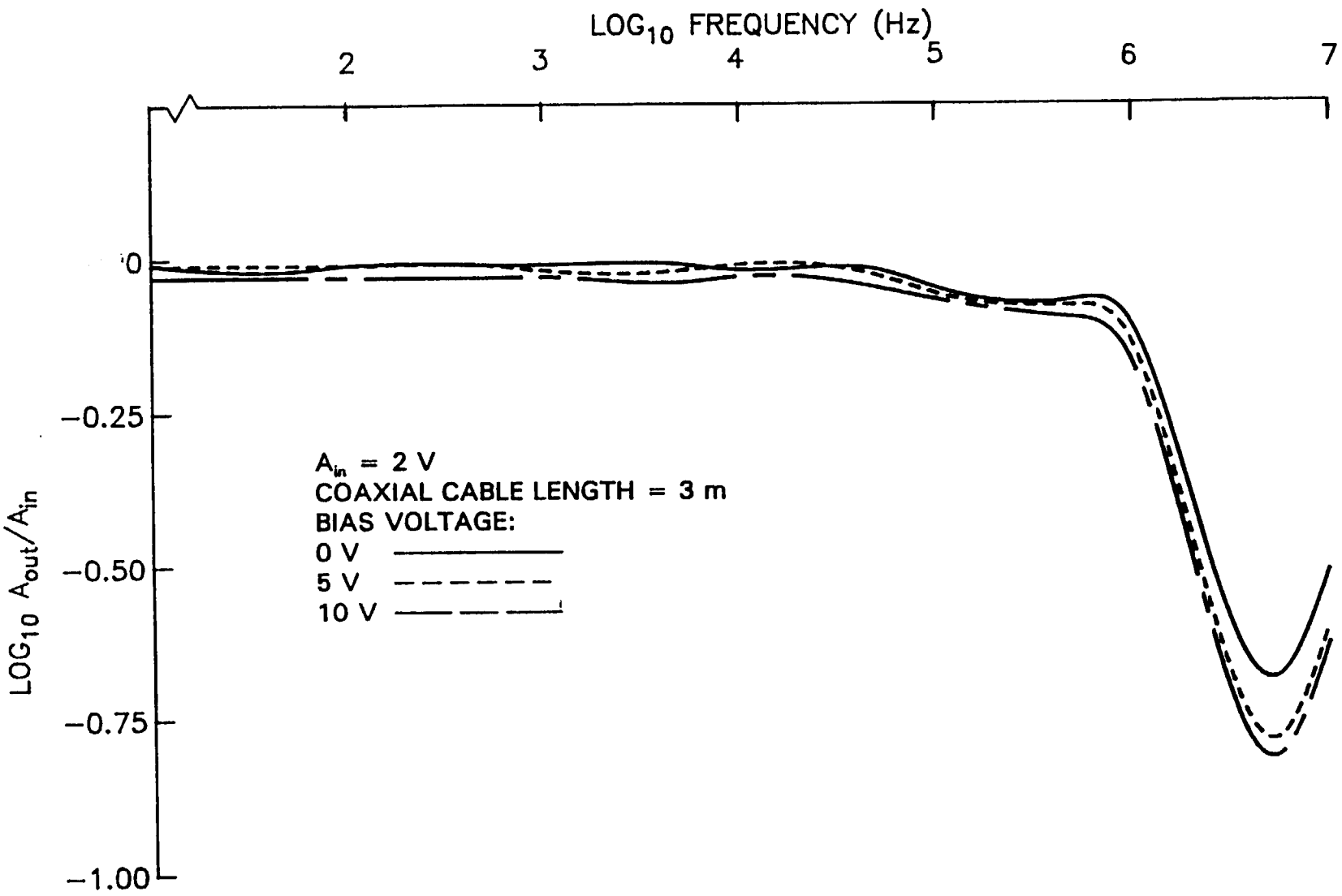

Fig. 9 Effect of the Bias Voltage on Frequency Response

log-log scale. Modest differences in the amplitude ratio are observed at the three different bias conditions, but they are not considered significant.

In some situations, coaxial cables with different lengths are used to connect the Langmuir probe to the bias supply. Hence, the effect of the length of this cable on the frequency response of the instrumentation was investigated. Typical results for 3 and 9-m-long cables are shown in Fig. 10 for the case where the bias voltage and wave amplitude were set at 5 V and 2 V, respectively. The dramatic difference in response of the two cables at 5.5 MHz appears to be related to signal reflection phenomena. Such reflections can occur at locations where coaxial cable impedances change and cause disturbances in the frequency response [11]. In the present case it appears that reflections in the 9-m-long cable may be inducing a resonance.

The maximum frequency detectable by the instrumentation was determined by a 256 kHz digitizing limit on the oscilloscope available to the project. The maximum frequency distinguishable by the FFT analysis is half of the digitizing limit, therefore the maximum frequency detectable is 128 kHz. Figures 6 through 9 show the response of the instrumentation is good at frequencies ranging to this value, so the investigation of the noise characteristics of the hollow-cathode-based plasma contactor to a 100 kHz frequency limit was conducted. The final configurations of the instrumentation are shown schematically in Fig. 11 where both schemes include the 4-pole (bandpass) filter which has been identified as the preferred unit. The instrumentation arrangement used to sense and record line noise given in Fig. 11a includes a 1Ω, current-sensing, shunt resistor which is positioned at one of the two locations identified in Fig. 3. Plasma noise measurements are made by biasing a 3.1 mm diam. stainless-steel, spherical Langmuir probe to the plasma potential at a

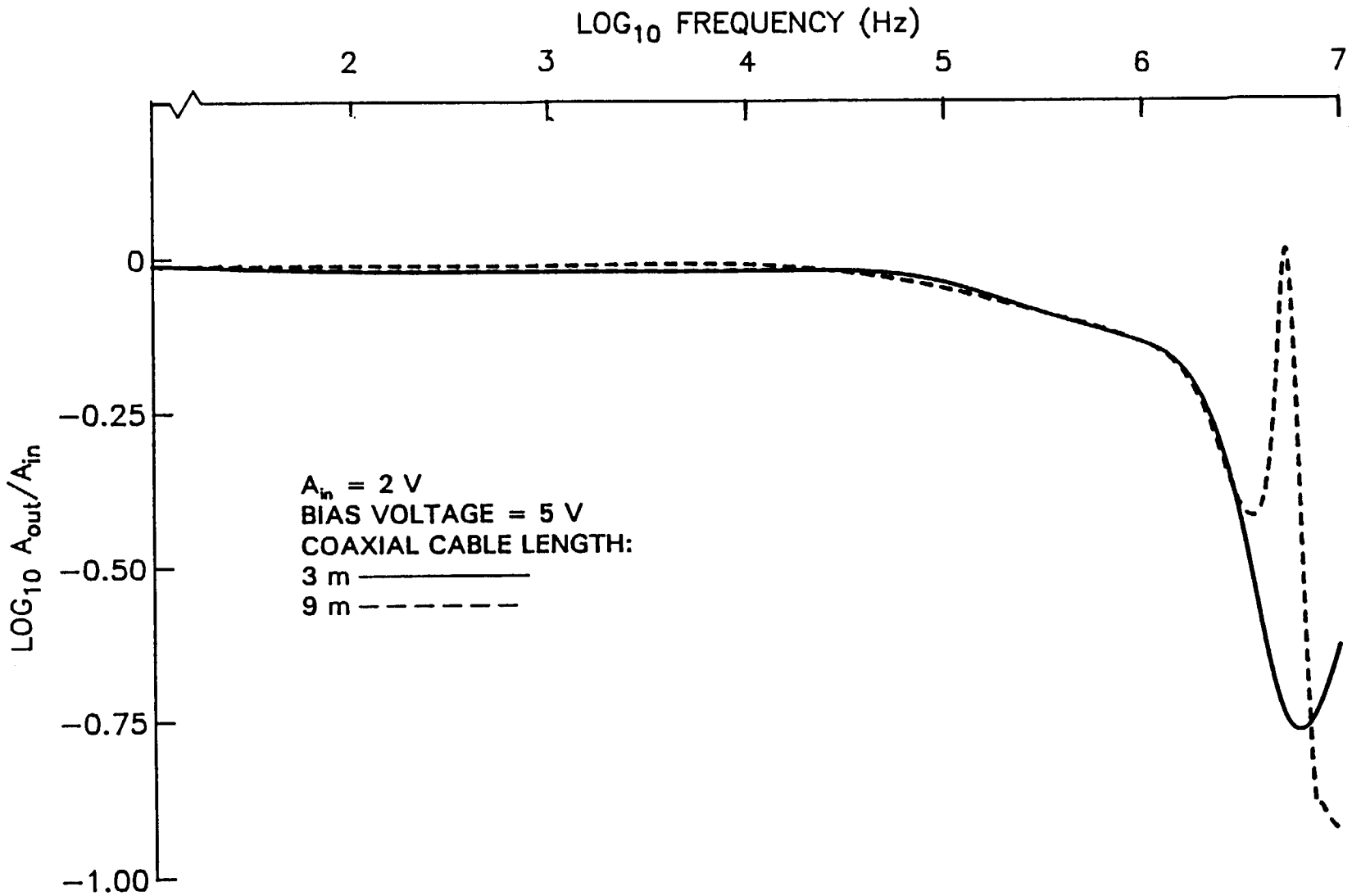

Fig. 10 Effect of Cable Length on Frequency Response

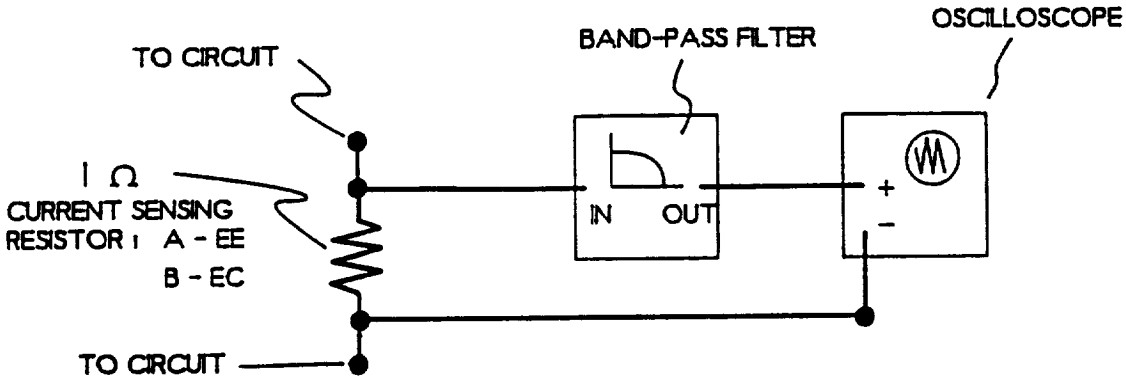

a) Instrumentation Used for Line Noise

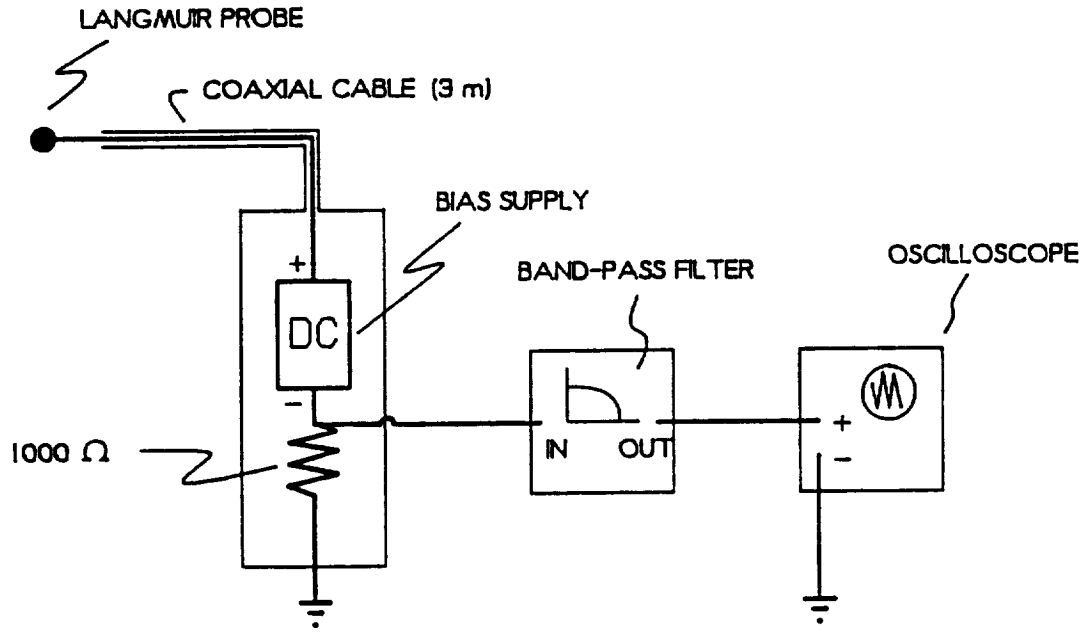

b) Instrumentation Used for Plasma Noise

Fig. 11 Final Instrumentation Schematics

particular location and then measuring current fluctuations across a 1000 Ω, shunt resistor, placed in series with the probe (Fig. 11b). Local plasma potentials were determined by using an emissive probe at the same location where plasma noise measurements were made.

As stated previously, it was decided that independent measurements should be made in three overlapping frequency ranges (0.01 to 1 kHz, 0.1 to 10 kHz and 1 to 100 kHz) to assure adequate attenuation of aliased signals and reasonable frequency resolution over the complete 0.01 to 100 kHz frequency range. Further, eight sets, or samples of noise data were taken in each frequency range to complete a measurement. Next, the FFT of each sample was taken, amplitudes for the various Fourier terms were determined, and the root-mean-square of these amplitudes were computed for each frequency range. The maximum theoretical error in the root-mean-square values determined from eight samples is $\sim 35\%$ [9]. This error can be reduced by taking more samples (the error is inversely proportional to the square root of the number of samples taken). In the present case, eight samples was judged to yield a reasonable balance between the time required to collect the data and the maximum error. Power spectral densities were computed from the FFT results by dividing the root-mean-square amplitude at a given frequency by the bandwidth associated with the measurements. As discussed in Appendix A, the bandwidth is determined by the window time used for each frequency range. Table 1 shows filter frequency ranges, sampling rates, cutoff frequencies, and window times used to cover the 0.01-to-100 kHz range investigated in this study.

Frequency Range of the Filter	Sampling Rate of Oscilloscope	Cutoff Frequency due to Sampling Rate	Window Time
10 to 1000 Hz	10.2 kHz	5120 Hz	0.05 s
0.1 to 10 kHz	102 kHz	51.2 kHz	0.005 s
1 to 100 kHz	256 kHz	128 kHz	0.002 s

Table 1. Sampling Rate and Frequency Information

Results

Line Noise Characteristics

Line noise measurements were made at several contactor operating conditions and power-spectral density data were calculated from them. A typical example of these data, obtained when the contactor was collecting 940 mA of current (J_{CE} = -940 mA) from the ambient plasma are given in Fig. 12. This figure shows the power spectral density reaches a broad peak near 1000 Hz and then exhibits a general decrease at a rate between 1 and 2 decades per decade of frequency above this frequency. Additional useful information can be obtained from the data in Fig. 12 by integrating under portions of the plot. For example, the area under the plot from 1 to 10 kHz is 4570 mA^2 so the root-mean-square of the current fluctuations, ΔJ_{rms}, for this frequency range is $(4570)^{1/2}$ = 67.6 mA, or ~7% of the collected current.

Typical examples of PSD plots obtained when emission current, J_{CE}, was varied over the range from 1000 mA of electron emission to 1000 mA of electron collection are shown in Fig. 13. The actual contactor-potential/emission current operating points associated with the PSD data are identified by the circular data points in the central, contactor performance plot. The PSD plot in the lower right corner (J_{CE} = -940 mA) is the one shown previously in Fig. 12. The PSD data in Fig. 13

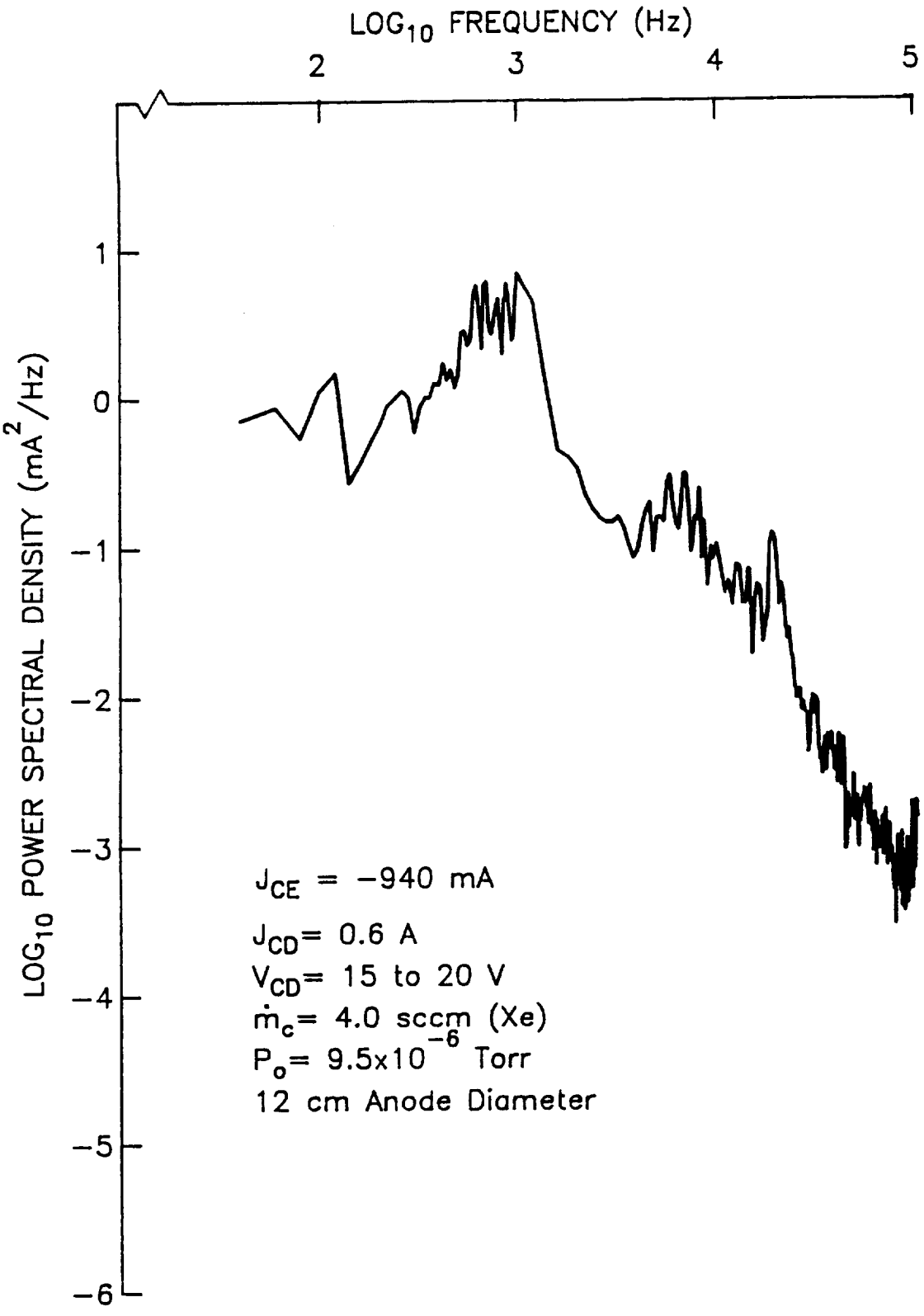

Fig. 12 Typical Electrical Line Noise

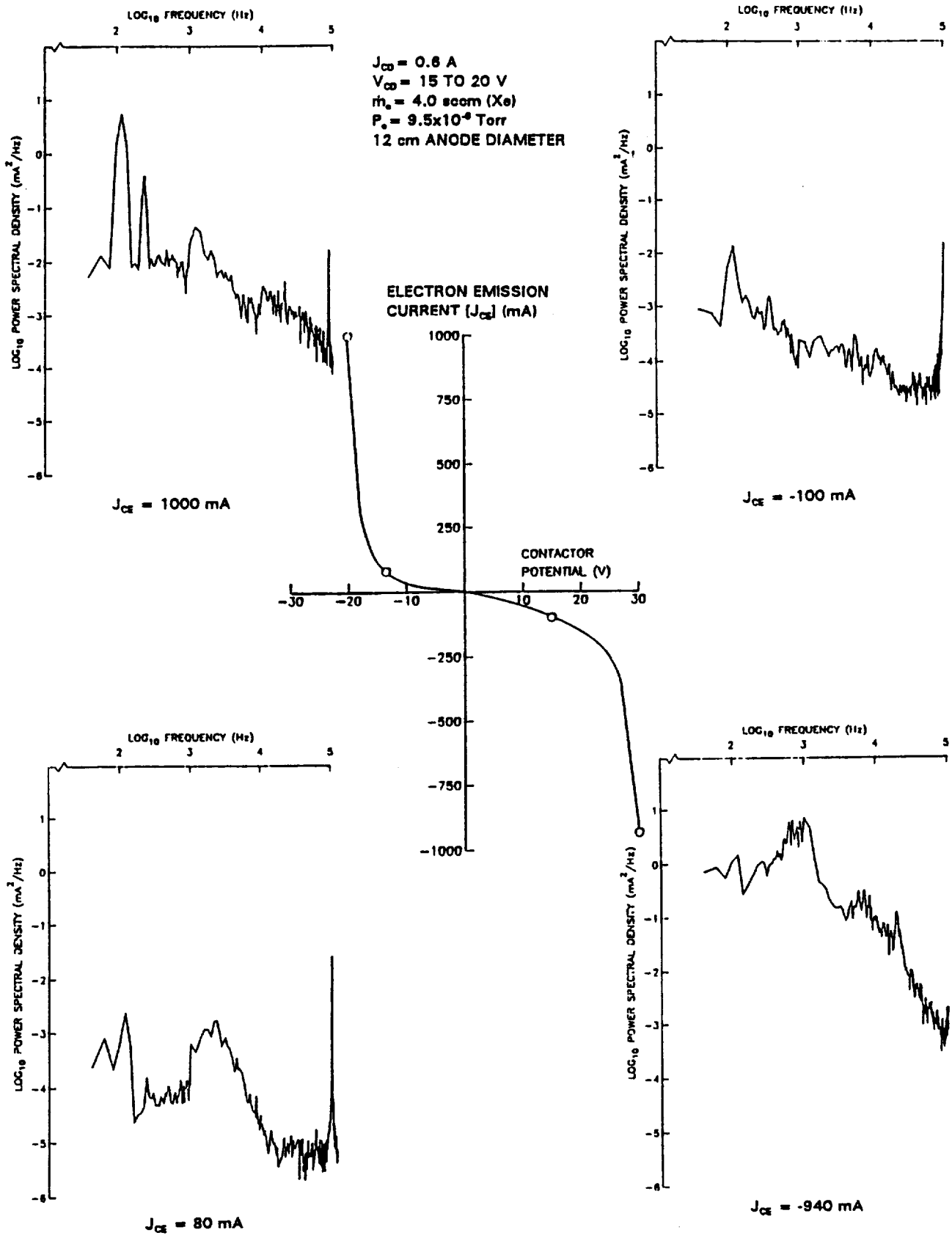

Fig. 13 Various Spectrum at Different Emission Currents

suggest that noise levels are generally 1) greater at the higher collection and emission currents and 2) lower for operation in the emission mode than they are for the collection mode. Resonances appear to be driven by 60 Hz noise from power supplies (e.g. the 120 and 240 Hz peaks for J_{CE} = 1000 mA) and possibly by ion-acoustic phenomena (1-kHz peaks are within the range of ion-acoustic phenomena for the plasma conditions and geometry involved). Peaks near 1 kHz, which seem to be present in three of the plots, are especially strong for the J_{CE} = -940 mA data. The peaks which appear at 100 kHz in three of the plots are near the limit of resolution of the oscilloscope used to make the measurements and their validity is considered questionable.

For a wide range of contactor emission currents, ΔJ_{rms} was calculated by integrating the PSD associated with each emission current for the two frequency ranges 0.01 to 1 kHz and 1 to 100 kHz. The results, which plotted in Fig. 14 as a function of J_{CE}, confirm the previously mentioned observation that 1) noise levels generally increase with emission or collection current magnitudes and 2) noise levels are generally lower for electron emission than they are for electron collection. However, they also show there are discontinuities in these trends. For example, the lower-frequency values of ΔJ_{rms} (upper plot) generally increase modestly with the magnitude of the electron-emission current J_{CE}. However, there is a sudden increase in ΔJ_{rms} for J_{CE} in the range between -300 and -500 mA. Similar behavior occurs in the higher-frequency range near a 300 mA electron-emission current (lower plot). It is suspected the transition to higher noise levels in the electron-collection regime (upper plot) was induced by contactor-power supply interactions accompanied by transitions into and from the ignited mode of contactor operation [3]. The reason for

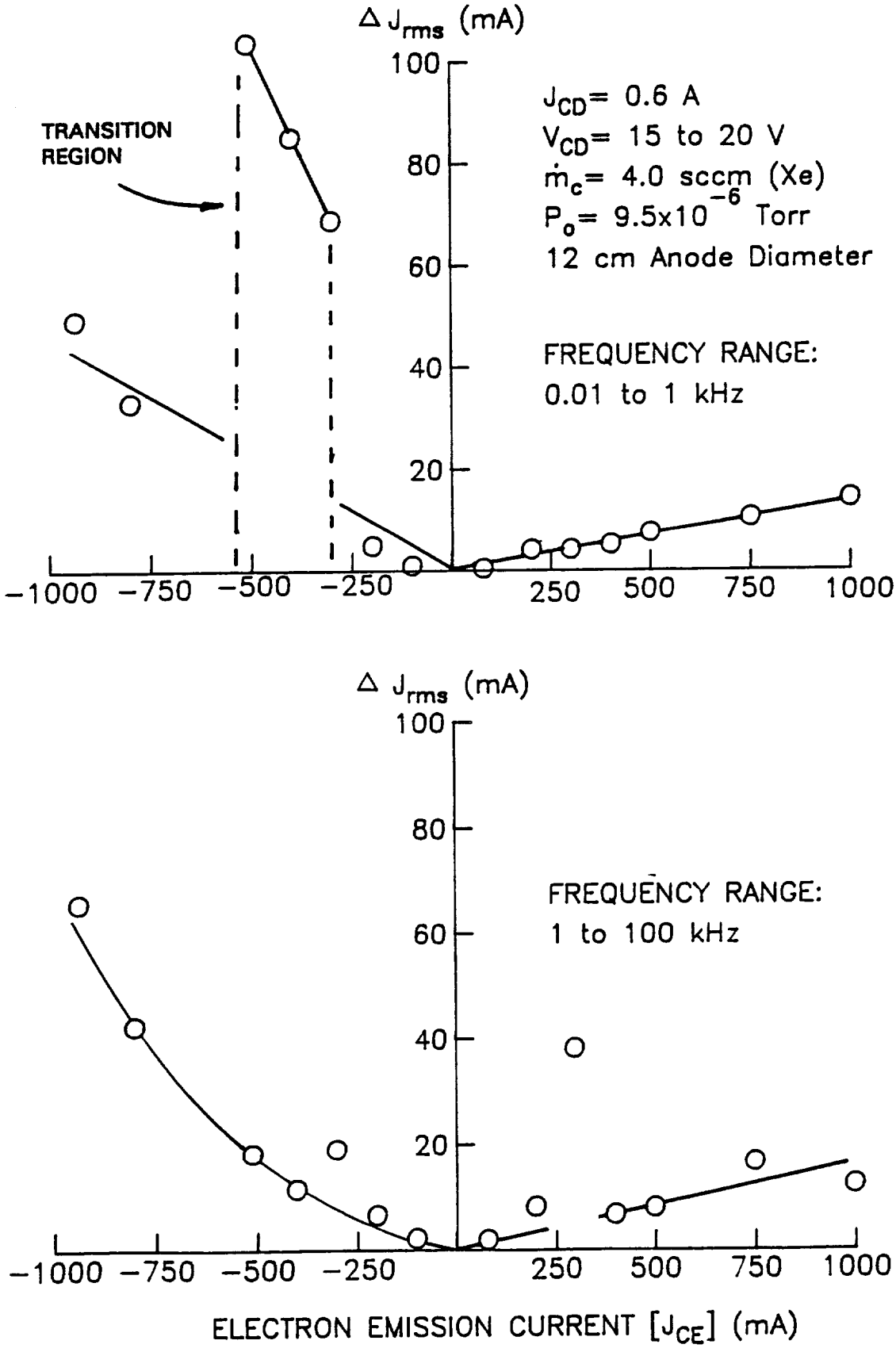

Fig. 14 Effect of Emission Current on Current Fluctuations

the other transition (at 300 mA in the high-frequency range) is uncertain. Except for these transition zones, it appeared that ΔJ_{rms} was proportional to the emission current in both frequency ranges with ΔJ_{rms} exhibiting the reasonable trend of decaying toward zero as J_{CE} was reduced. Typically, noise levels in the emission mode are $\sim$2% of the emitted current while in the collection mode the noise can be as low as 2% or as great as 20% of the collected current.

Plasma Noise Measurements

Noise measurements were made in the plasma downstream of a contactor collecting electrons using the instrumentation shown in Fig. 11b. A typical experiment, which was conducted with the plasma contactor collecting 500 mA of electron current (J_{CE} = -500 mA) from the simulator, yielded the plasma potential profile shown in Fig. 15. Here, the plasma potential, V_p, undergoes a 10 V drop in a double layer located $\sim$15 cm downstream from the contactor. The triangles in Fig. 15 indicate where plasma noise measurements were made.

Current fluctuations to the Langmuir probe were recorded on the oscilloscope and as before, the FFT computer program was used to analyze the data to compute PSD and ΔJ_{rms}. These current fluctuation results could have been plotted directly, but it was considered more useful to present the data as fluctuations in the properties most likely to have induced the current fluctuations, namely plasma potential and/or density. Potential fluctuation signals were computed from the current data using the slope of a Langmuir probe voltage/current curve at plasma potential and assuming density did not fluctuate, hence they represent maximum potential fluctuations. Conversely, maximum plasma density fluctuations were determined by assuming potentials did not fluctuate. For both cases, the electron temperature was assumed to

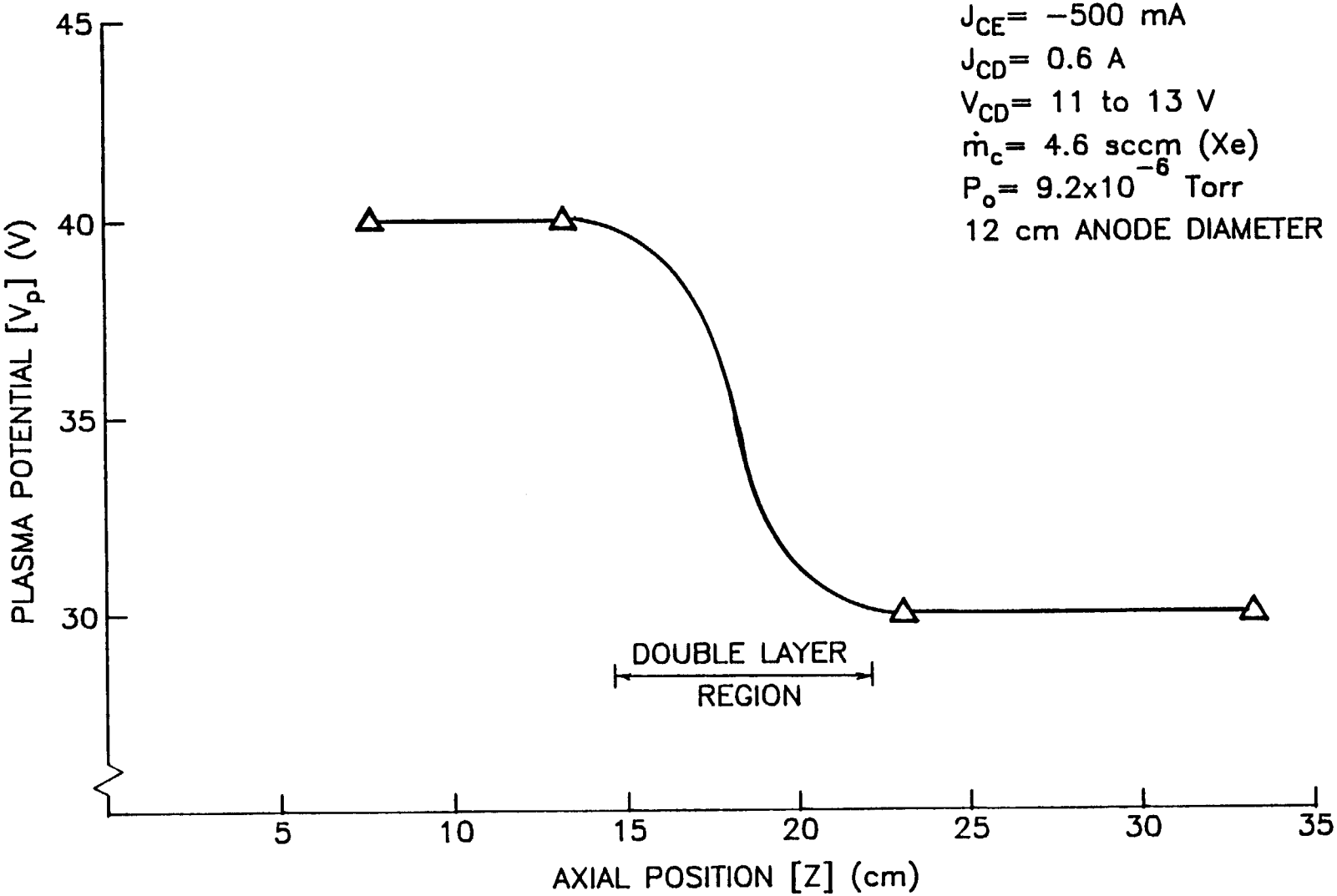

Fig. 15 Plasma Potential Profile

remain relatively constant.

The PSD data plotted in terms of plasma density and plasma potential at a location just downstream of the contactor (Z = 7.5 cm) are shown in the dual y-axis plot in Fig. 16a. Here the mean-squared-density per unit bandwidth (left side in units of cm^{-6}/Hz) and the mean-squared-potential per unit bandwidth (right side in units of V^2/Hz) are plotted as functions of frequency on a log-log scale. The data in the figure show evidence of significant noise at 60 and 120 Hz (probably induced by the contactor power supplies) in addition to components at 700 Hz and 13 kHz. Further downstream, at Z = 13 cm (Fig. 16b), the data indicate the same signals of 60, 120, and 700 Hz but the 13 kHz signal found at Z = 7.5 cm (Fig. 16a) is not present and the reason why the signal would appear at one location and not the other is unknown. The noise data obtained downstream of the double layer (Z = 23, 33 cm) are presented in Fig. 17. They contain the same PSD component at 700 Hz, in addition to strong components at 3900 Hz (Fig. 17a) and 2800 Hz (Fig. 17b). Frequencies in the 700 to 4000 Hz range are consistent with waves that propagate at the ion-acoustic velocity and are reflected off of structure, such as the vacuum chamber walls located on the order of a meter from the double layer.

The ratio of the root-mean-square current fluctuations integrated over a prescribed frequency range, ΔJ_{rms}, to the mean current to the probe at plasma potential, J_p, is also descriptive of plasma noise. The square of this ratio is, in fact, proportional to the ratio of turbulent energy-to-mean thermal energy in the plasma [12]. The data of Figs, 16 and 17 have been re-plotted in terms of this ratio for low and higher frequency ranges (0.01-to-1 kHz and 1-to-100 kHz, respectively) in Fig. 18. From this figure it is apparent that, 1) modest noise is produced in the low-

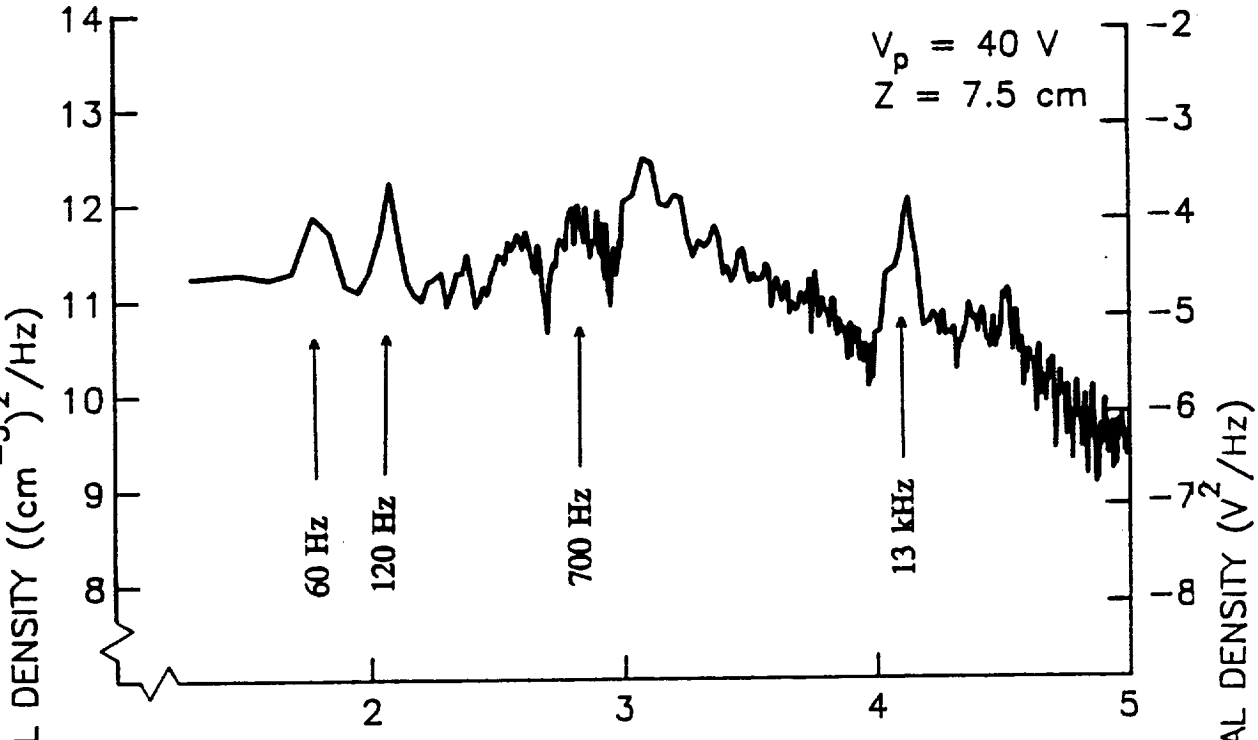

a) Probe near Contactor on ℄

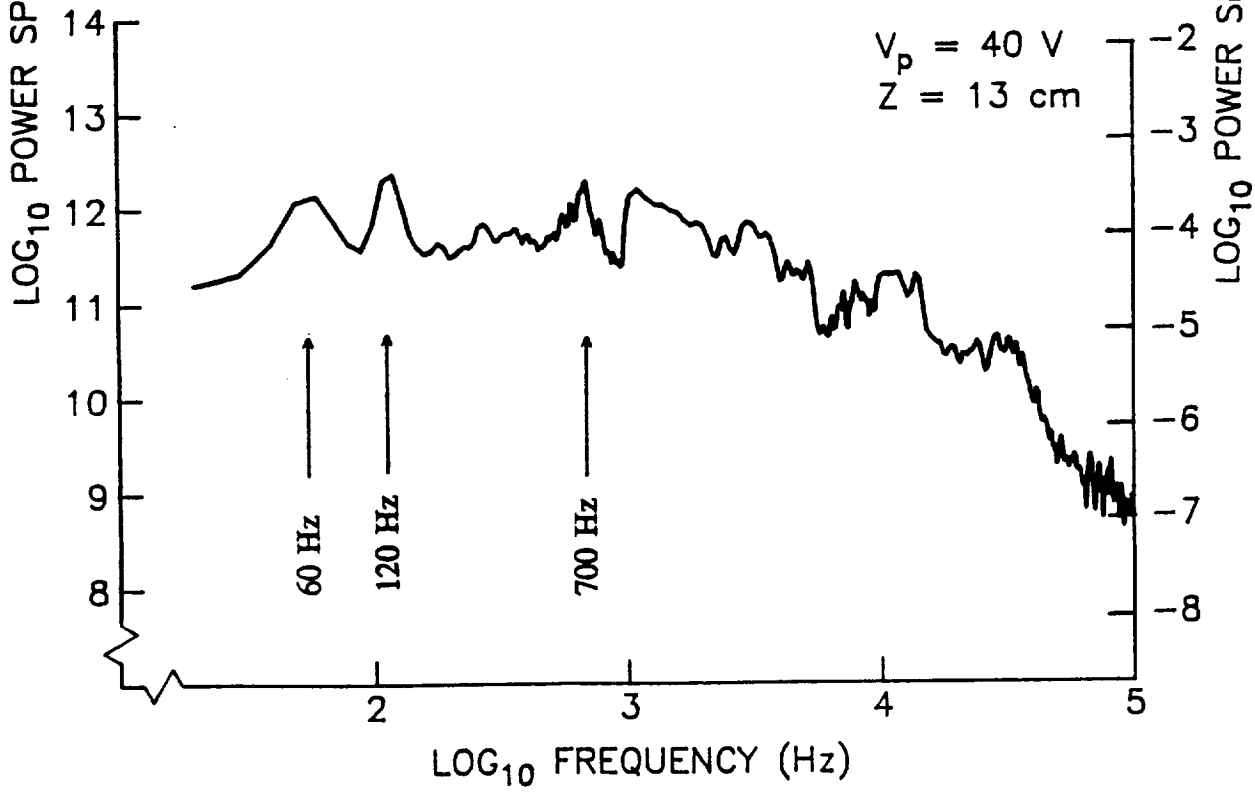

b) Probe near Upstream Edge of Double Layer on ℄

Fig. 16 Power Spectral Density Plots

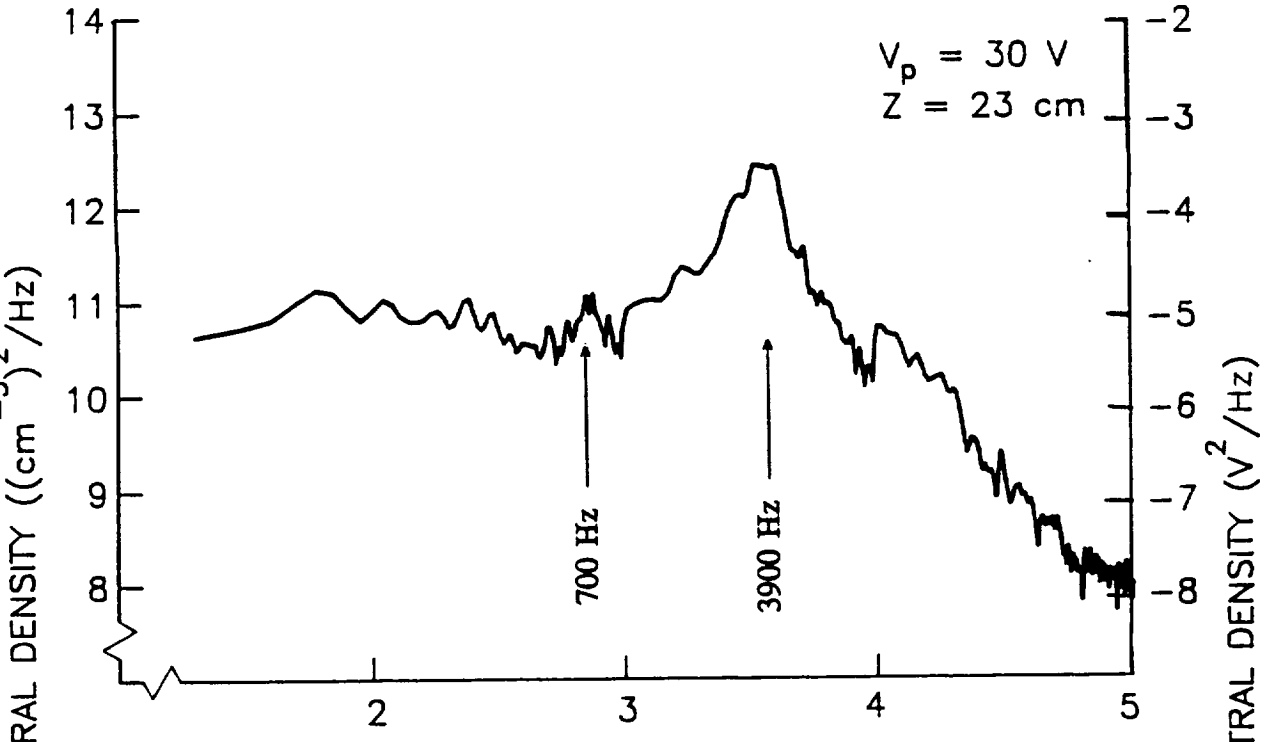

a) Probe near Downstream Edge of Double Layer on ¢

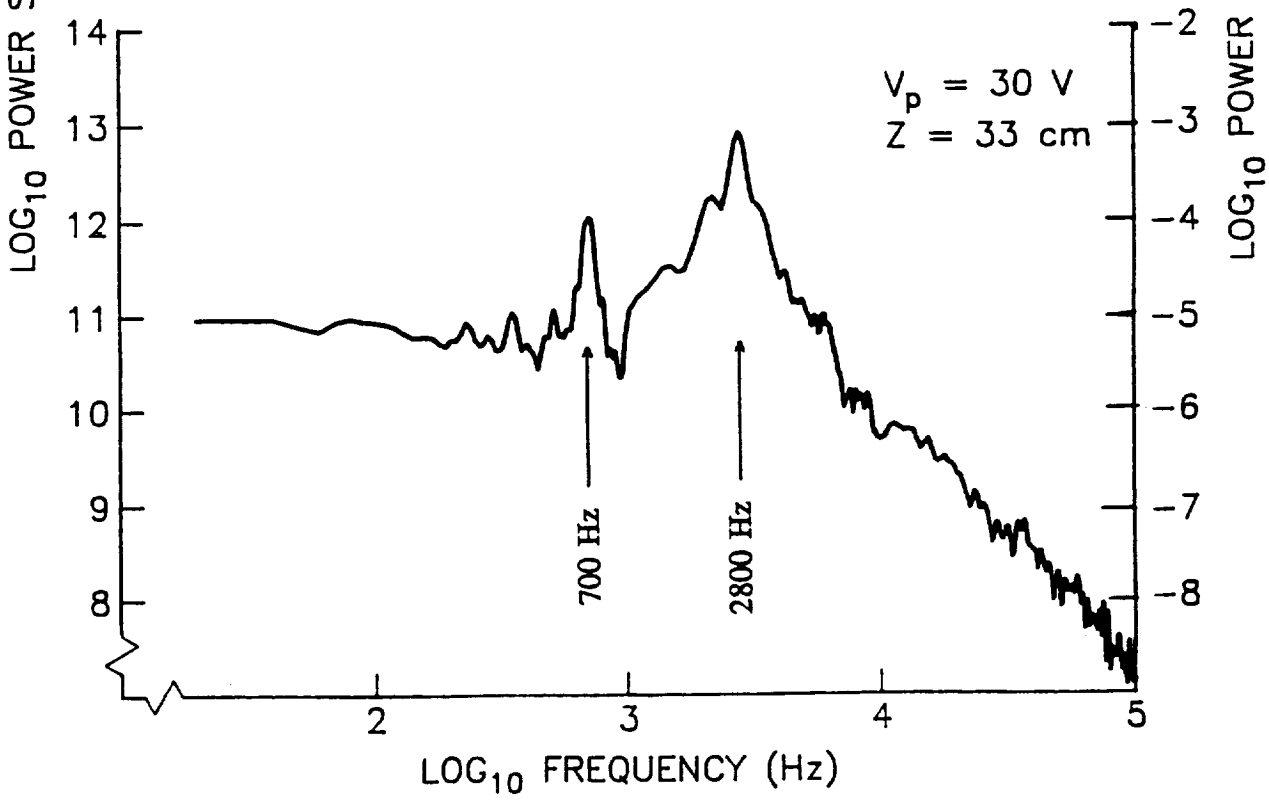

b) Probe in Ambient Plasma on ¢

Fig. 17 Power Spectral Density Plots

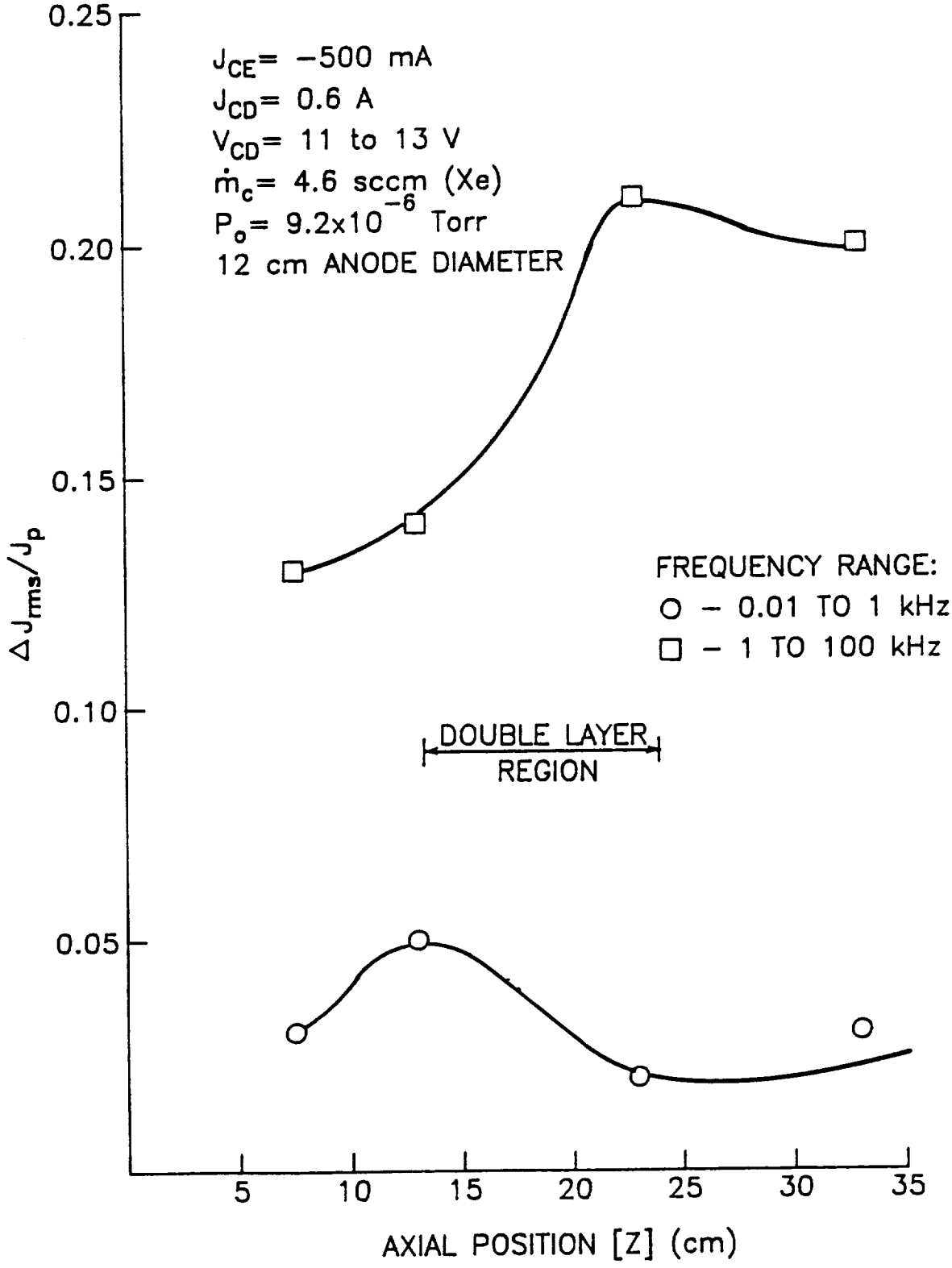

Fig. 18 Current Fluctuations as a Function of Position

frequency range, 2) this noise peaks near the upstream boundary of the double layer, 3) high-frequency noise is more substantial than low-frequency noise and 4) low-frequency noise peaks near the downstream boundary of the double layer.

Discussion

Results from several experiments suggest noise in the plasma contactor return line is generally greater when the contactor is collecting electrons than when it is emitting them. The experiments reveal noise levels are roughly proportional to the amount of current collected or emitted except for a few transition regions where sudden increases in noise are observed. When the contactor is collecting electrons, these noise levels generally vary between 2% and 20% of the collected current. When the contactor is emitting electrons, the noise is $\sim 2\%$ of the emitted current. The 20% noise levels in the electron collection mode could be due to power supply interference possibly coupled to the transition between the un-ignited and ignited modes [3] of contactor operation.

Plasma noise measurements reveal density and/or potential fluctuations that are probably driven by the harmonics of 60 Hz power supply noise. They also reflect higher frequencies (in the order of kHz) which are consistent with waves propagating between plasma and physical structures at the ion acoustic velocity. In this case, the plasma and physical structures could be the double layer and vacuum-chamber walls, respectively [13]. In a space environment, this mechanism of noise production could be subdued because any structure adjacent to the contactor and double layer would be much more transparent than the vacuum chamber which completely surrounds the ground-based experiments.

The work reported herein in considered preliminary and incomplete.

Additional experiments will focus on 1) plasma noise produced by contactors emitting electrons, 2) the effects of contactor operating conditions on general noise levels, and 3) the emission and collection currents at which plasma noise levels undergo transitions to the higher ($\sim 20\%$ of mean plasma current) values. Additional effort will focus on the mechanisms through which the noise is created; this is expected to lead to an understanding of the extent to which noise measured in ground-based experiments will develop in space.

CONSTRUCTION AND TESTING OF A PROBE POSITIONING SYSTEM

Brett Buchholtz

A probe-cart system for positioning various probes within the vacuum chamber which houses plasma-contacting experiments at Colorado State University has been designed, constructed, and tested. This system is shown schematically with front, side, and top views in Fig. 19. The wheels on the cart from which the probes are supported move axially along the two stainless steel guide tracks in response to forces exerted via the wire rope shown in the figure. This rope system, which can pull the cart in either axial direction, is driven via a shaft and chain drive from outside the tank. A small DC motor, mounted on the cart, rotates a cantilevered support arm which in turn holds a probe in the manner suggested by the figure. The motor and its controller are shielded to prevent electrical noise radiated by the motor from interfering with the probe position sensing apparatus and/or the plasma measurements made by the probes. Axial and radial probe positions are sensed as voltage drops across potentiometers and are transmitted outside the vacuum tank. A wire retrieval system (not shown in the figure) retracts (or feeds) the motor control, position sensing, and probe wires, which are all attached from an electrical feed-through to the moving cart.

After the cart system had been designed and built, an emissive probe was mounted to the cart. The probe was used to measure the plasma potential variation along the tank centerline through a plasma double layer produced downstream of a contactor collecting a 210 mA of electron current (J_{CE} = -210 mA). A centerline plasma-potential profile was also measured in this same plasma environment using an

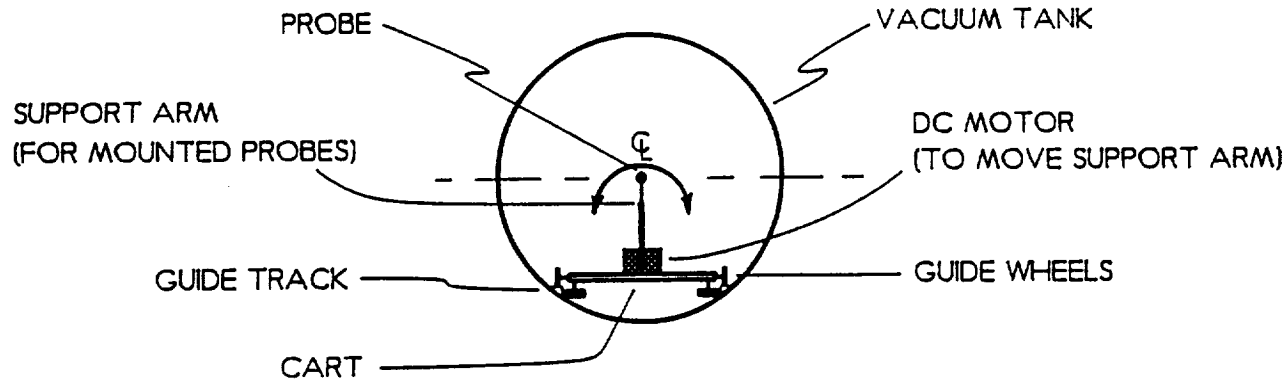

a.) FRONT VIEW

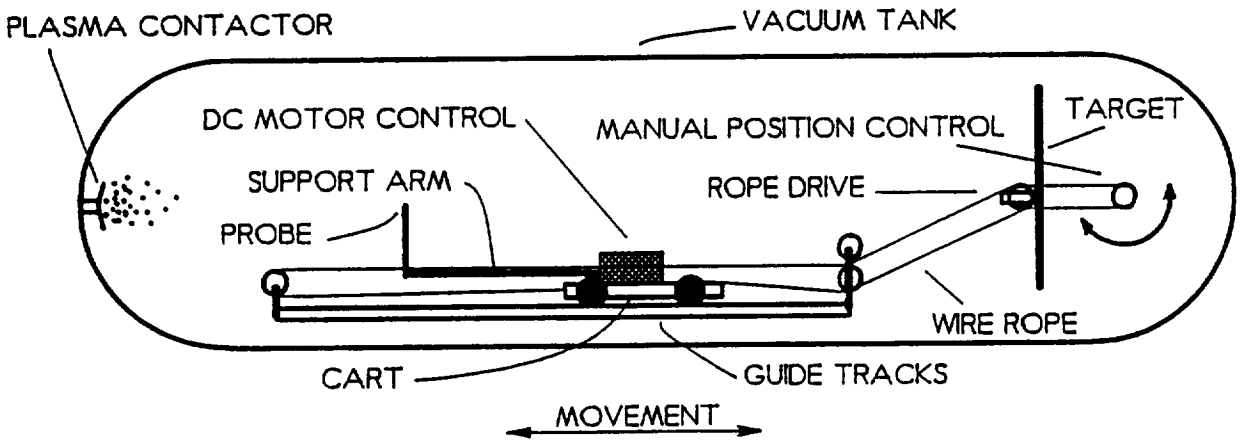

b.) SIDE VIEW

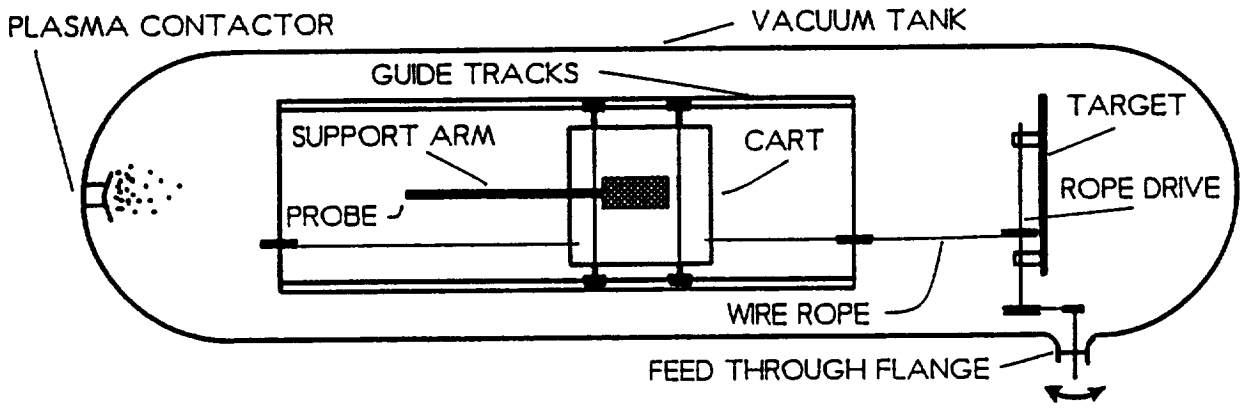

c.) TOP VIEW

Fig. 19 Probe Positioning System Schematic

essentially identical emissive probe mounted on the previous positioning system (the long push-rod assembly illustrated in Fig. 1). Identical probe heating and data-acquisition apparatus was used for both measurements. The resulting potential profiles are compared as the solid and dashed lines shown in Fig. 20. These lines show a potential difference of a few volts, but they are otherwise quite similar. The small differences in the profiles could be due to slight differences in contactor operating conditions, probe construction, and/or axial probing trajectories. In any case, the results are considered to agree sufficiently well so it can be concluded the probe-cart system yields plasma-potential data similar to those obtained using the old system. The new probing system is better supported and more stable, therefore it is expected to yield more accurate results in regions far downstream of the contactor.

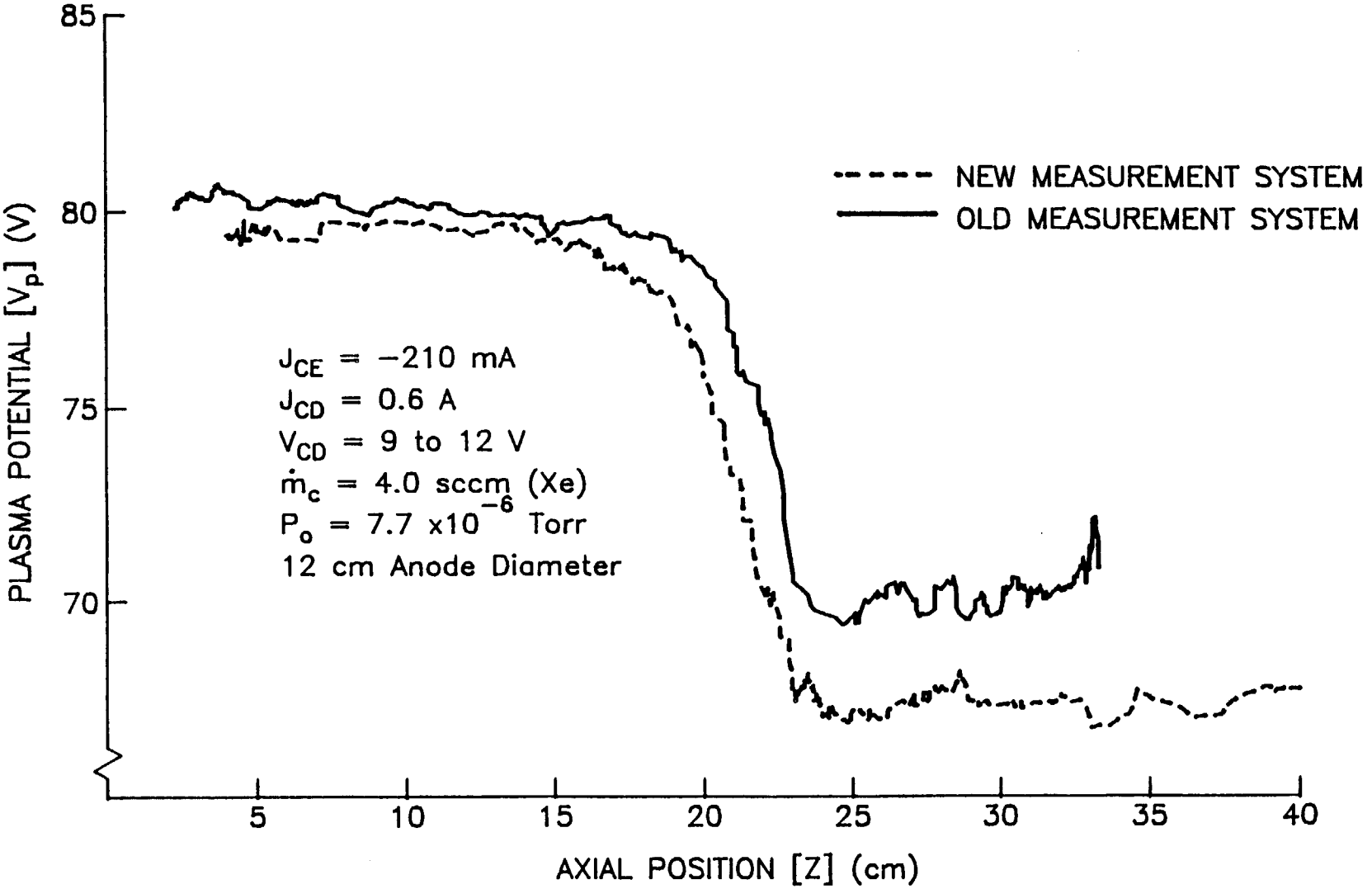

Fig. 20 Plasma Potential Profile

References

1. Williams, John D., "An Experimental Investigation of Hollow Cathode-Based Plasma Contactors," NASA CR-187120, May, 1991.

2. Williams, John D., "Plasma Contactor Research," P.J. Wilbur, ed., NASA CR-187097, Jan. 1991.

3. Williams, J. D., and P. J. Wilbur, "Experimental Study of Plasma Contactor Phenomena," Journal of Spacecraft and Rockets, V. 27, N. 6, 1990, pp. 634-641

4. Davis, V. A., et al, "A Model of Electron Collecting Plasma Contactors," Submitted to Journal of Spacecraft and Rockets, 1989

5. Davis, V. A., and I. Katz, "Plasma Sources for Active Charge Control," 1989 Spacecraft Charging Technology Conference, S-CUBED Division of Maxwell Laboratories, Inc., La Jolla, CA

6. Hastings, Daniel E., and Robie I. Samanta Roy, "A Brief Overview of Electrodynamic Tethers," SPPL-91-0007, M.I.T., 1991

7. Press, William H. et al, Numerical Recipes: The Art of Scientific Computing, Fortran Version, Cambridge University Press, New York, 1989, Chap. 12

8. Chapra, Steven C. and Raymond P. Canale, Numerical Methods for Engineers, 2nd Ed., McGraw-Hill, New York, 1985, Chaps. 13 & 14.

9. Bendat, Julius S. and Allan G. Piersol, Random Data: Analysis and Measurement Procedures, 2nd Ed., John Wiley and Sons, New York, 1986, Chaps. 1,8,10, & 11.

10. Horowitz, Paul and Winfield Hill, The Art of Electronics, Cambridge University Press, New York, 1980, Chap. 4.

11. Ramo, Simon et al, Fields and Waves in Communication Electronics, John Wiley and Sons, New York, 1965, Chaps. 1,6, &9.

12. Hollenstein, Ch., and M. Guyot "Experiments on Potential Gradients in a Current-Carrying Plasma. II. Turbulence," Phys. Fluids, V. 26, N. 6, 1983, pgs. 1606-1615

13. Chen, Francis F., Introduction to Plasma Physics and Controlled Fusion, 2nd Ed., Vol. 1, Plenum Press, New York, 1984, Chap. 4.

14. Ramirez, Robert W., "The fast Fourier transform's errors are predictable, therefore manageable," Electronics, June 13, 1974.

APPENDIX A

ACQUIRING AND INTERPRETING LINE- AND PLASMA-NOISE DATA

by Brett Buchholtz

The investigation of electrostatic noise requires an examination of fluctuating signals in order to determine the possible source(s) and/or the production mechanism(s) related to the noise. For example, the current drawn to a Langmuir probe from a plasma generally fluctuates about a mean value because plasma density, potential, and/or temperature are fluctuating at the probe. In order to gain understanding of the phenomena that induce these fluctuations, it is useful to examine the frequency spectra (spectral composition) of the fluctuations. Such spectra can be obtained from experimental Langmuir probe current data using Fourier transforms. Recall, a Fourier transform takes a continuous function, or signal, in the time domain and converts it into a function in the frequency domain. Figure A1a illustrates a fluctuating signal, in this case a sine wave in the time domain which has amplitude A_1, frequency f_n, and period τ, where $\tau = 1/f_n$. The sine wave also has a phase shift ϕ, but this parameter will generally be unimportant in the applications being considered. The sine wave of Fig. A1a is represented in the frequency domain by the plot of amplitude as a function of frequency shown in Fig. A1b.

In order to apply the Fourier transform procedure, a continuous function over an infinite time interval is required. Data are, however, only collected over a finite interval. A discrete Fourier transform (DFT) facilitates the conversion of a signal in a finite-time domain, represented by a discrete number of data points, into the

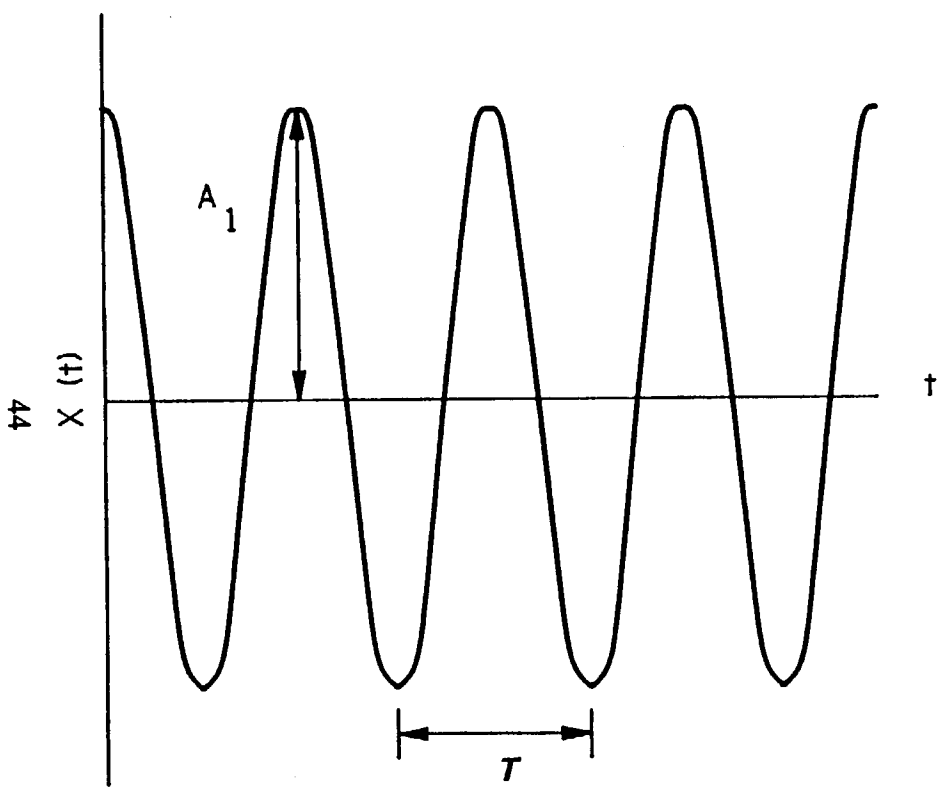

a) Time Domain: $X(t) = A_1 \sin(\omega_n t + \phi)$

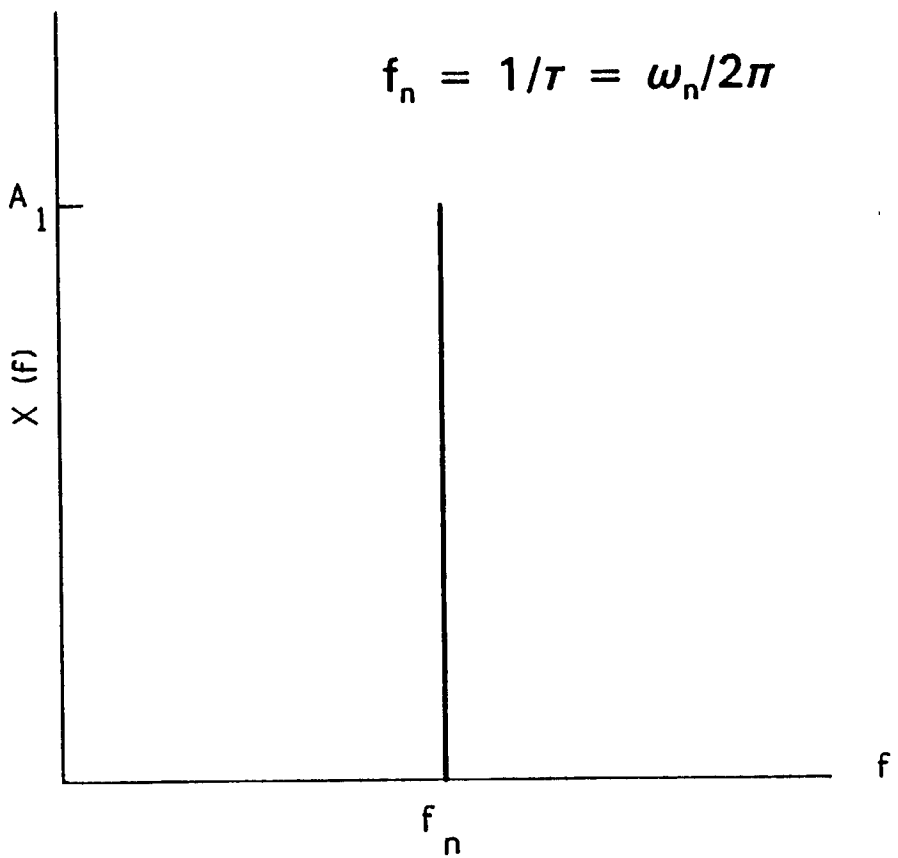

b) Frequency Domain Characteristics (Spectrum)

Fig. A1 Sinusoidal Function Example

frequency domain. There have been algorithms developed to estimate the DFT, however, depending upon the number of data points involved, they can require excessive amounts of computational time. The fast Fourier transform (FFT) is an algorithm designed to compute the DFT more efficiently (i.e. in less time) [8,9]. Therefore, a FFT can be used to convert a signal, represented by discrete data points, collected over a finite-time interval into its frequency components rapidly. There are two features of FFT's, namely windowing and aliasing, which can introduce errors into the results and should, therefore, be understood before one attempts to use the FFT.

Windowing

The concept of windowing is illustrated by the various plots shown in Fig. A2. First, consider the continuous signal shown in Fig. A2a and the window (a unit step function of duration T), shown in Fig. A2c, through which the data are to be collected. The result of multiplying the continuous signal and the window is pictured in Fig. A2e. The window passes the full amplitude of the original signal for a finite duration and it is this portion of the signal which the FFT algorithm uses. Fast-Fourier-transform analysis assumes the input signal being used is continuous in the time domain so for the present case, where the window has passed only a finite segment of the continuous signal, the windowed signal is assumed to repeat. The ideal Fourier transform of the sine wave (Fig. A2a) is represented by the spike shown in Fig. A2b. The Fourier transform of the unit step function, on the other hand, exhibits a peak at zero frequency coupled with some roll off into higher frequencies (Fig A2d). When the two transforms (Fig. A2b and A2d) are convoluted in the frequency domain, the fast Fourier transform of the non-continuous signal is obtained

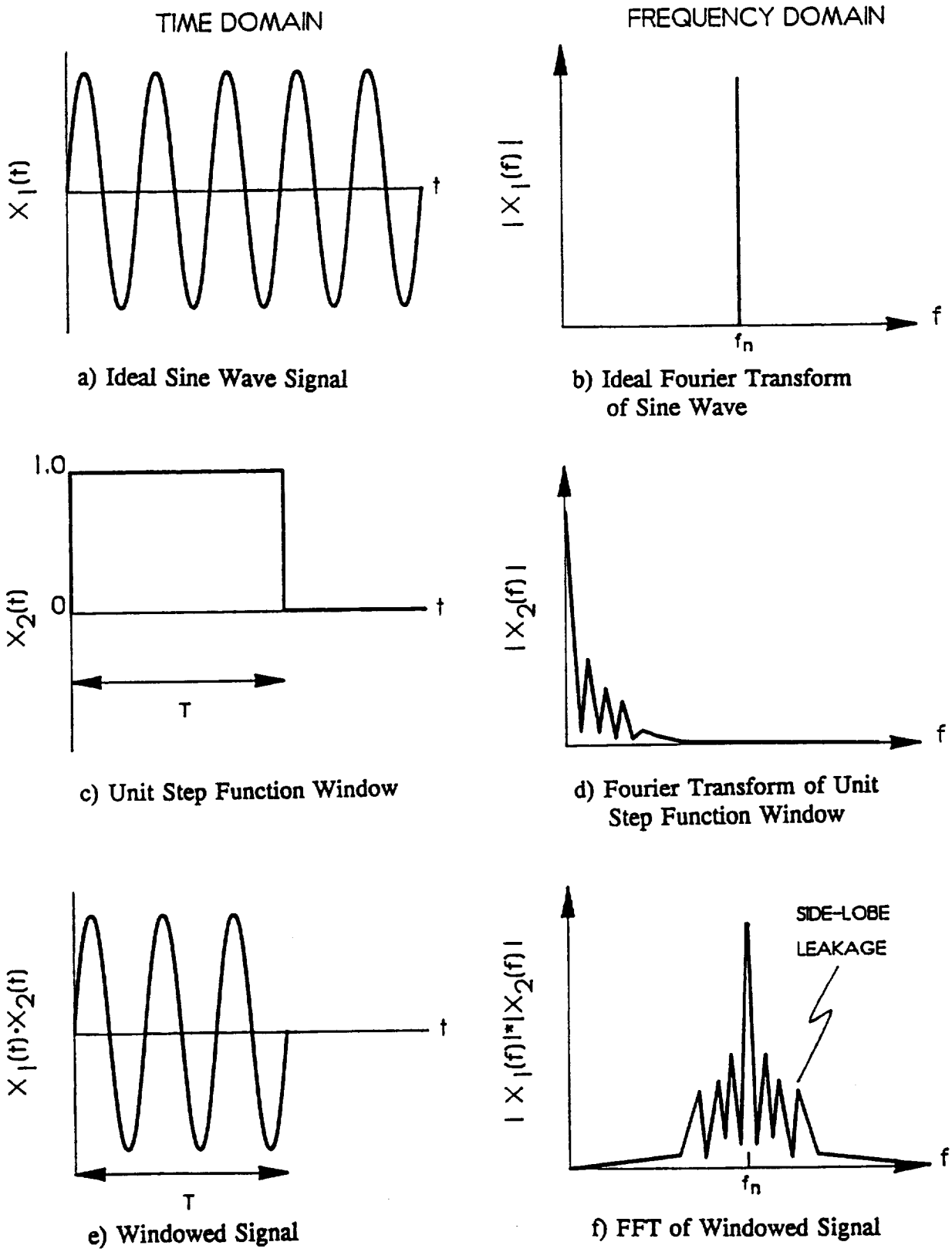

Fig. A2 The Effect of a Unit Step Function Window on the FFT

(Fig. A2f). This transform contains leakage, known as side-lobe leakage, which occurs from inputing the abrupt, windowed signal into the FFT. Side-lobe leakage is not present in the ideal transform and is, therefore, erroneous and it should be removed.

In order to reduce side-lobe leakage, other types of windows can be used. For example, Fig. A3a shows the same continuous signal (i.e. the one of Fig. A2a) which will be convoluted with another window known as the Hanning, or cosine-squared window (Fig. A3c). The product of these two signals (Fig. A3e) is tapered i.e. its amplitude varies with time. Hence, using this window to pass the data into the FFT causes attenuation of the ripple associated with abrupt changes at the window edges thereby reducing the amplitude of the side-lobe leakage. In the frequency domain, the Fourier transform of the continuous signal is again represented by a spike (Fig. A3b). The transform of the Hanning window (Fig. A3d) has less roll off than the unit step function transform (Fig. A2d). More importantly, the fast Fourier transform of the non-continuous, windowed signal, depicted in Fig. A3f, exhibits reduced side-lobe leakage. The Hanning window does produce overall amplitude loss in the FFT but this loss is predictable and, therefore, correctable [9].

Proper windowing reduces side-lobe leakage into other frequencies thereby yielding a high resolution spectral plot (i.e. one in which amplitudes associated with two similar frequency components, which are close together, can be resolved). Thinking of windowing as the amplitude per unit time used in the FFT algorithm, one observes that greater window amplitudes near the window edges induces greater side-lobe leakage. There are many different windows [14] and the preferred one depends on the resolution required. The Hanning window is commonly used for the FFT

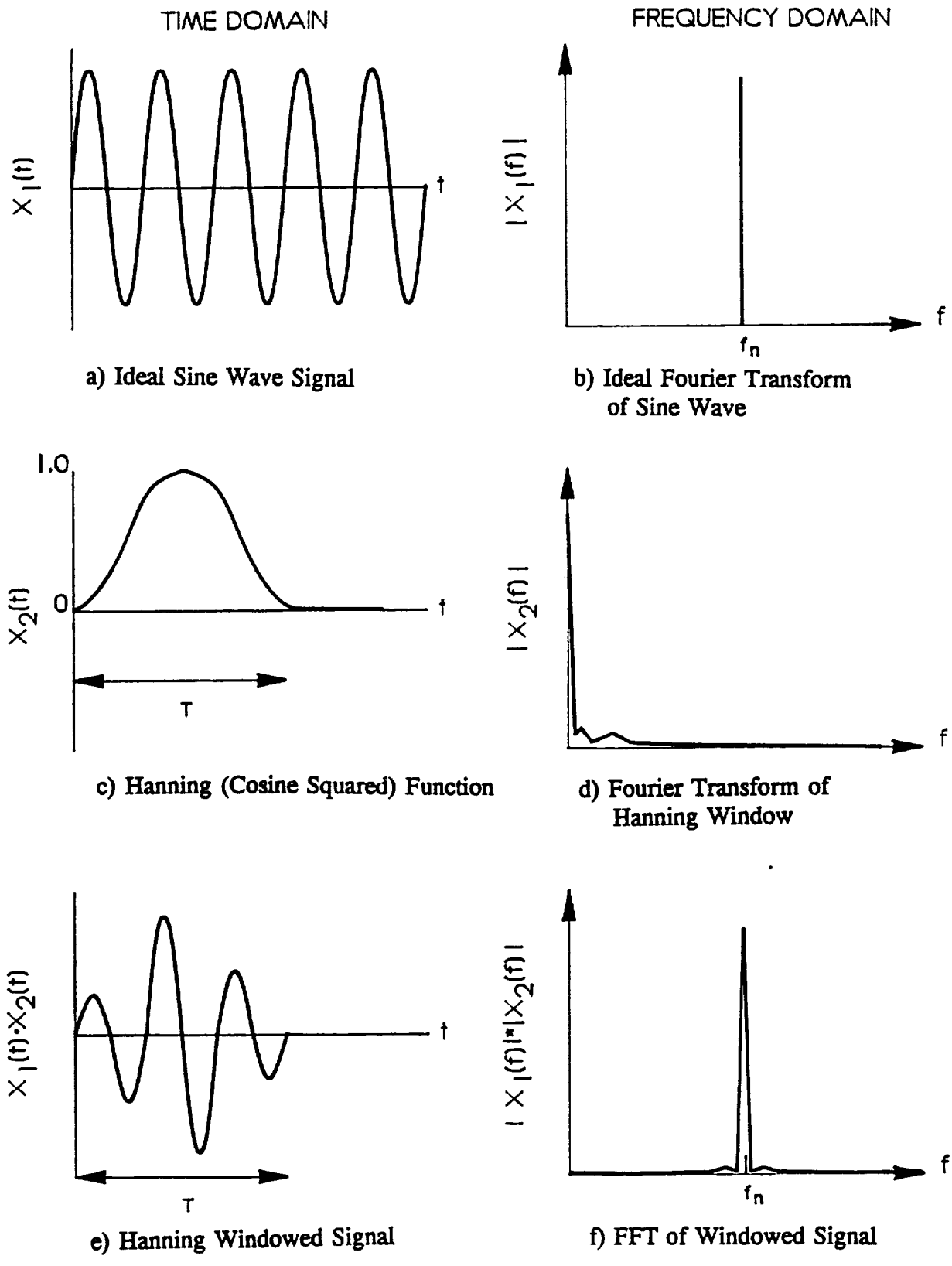

Fig. A3 The Effect of a Hanning Window on the FFT

because it yields acceptable resolution and, therefore, is used in the analyses presented in this report.

Aliasing

Aliasing, like windowing, yields false amplitudes in a spectrum but, unlike windowing, these false amplitudes tend to appear at frequencies far from the true frequency rather than as adjacent, roll-off signals. Hence, these false amplitudes are more difficult to identify and eliminate. Errors due to aliasing are generally prevented by using both mathematical (transform-related) and physical (raw data collection-related) procedures. The mathematical procedures exploit the fact that the FFT uses discrete data points which are sampled from the input signal. Aliasing can occur when an insufficient number of data points are collected (sampled). For example, Fig. A4a depicts a sine wave, with frequency, f_n, being sampled at rate which yields the five solid points indicated. When these are the only data analyzed, a false frequency is detected in the frequency domain (Fig. A4b). This can be prevented by sampling at a higher rate. For instance, the minimum sampling rate required to prevent aliasing is determined by the Nyquist criterion [7,9] and is equal to $2f_n$ where f_n is the maximum frequency sensed in the data. When this condition is invoked, the data points in Fig. A4c are obtained and the proper spectral plot (Fig. A4d) is realized.

If a signal contains more than one frequency component, aliasing is prevented by sampling at a rate greater than or equal to $2f_c$, where f_c is defined as the cutoff frequency and is the highest frequency component in the signal. The cutoff frequency, f_c, is directly related to the number of data points taken in the finite time T (the window time). For example, Fig. A5a shows a spectrum of a signal which

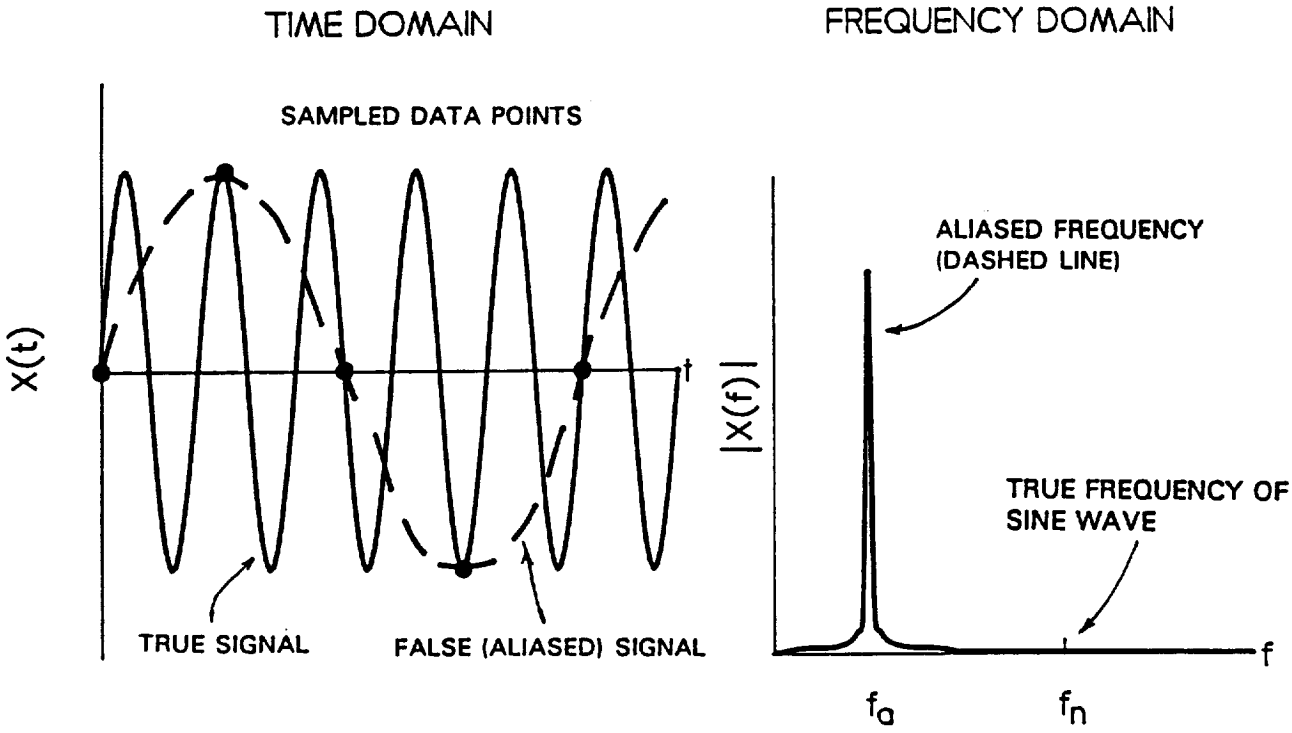

a) Ideal Sine Wave Sampled at a Low Rate

b) FFT at a Low Sampling Rate

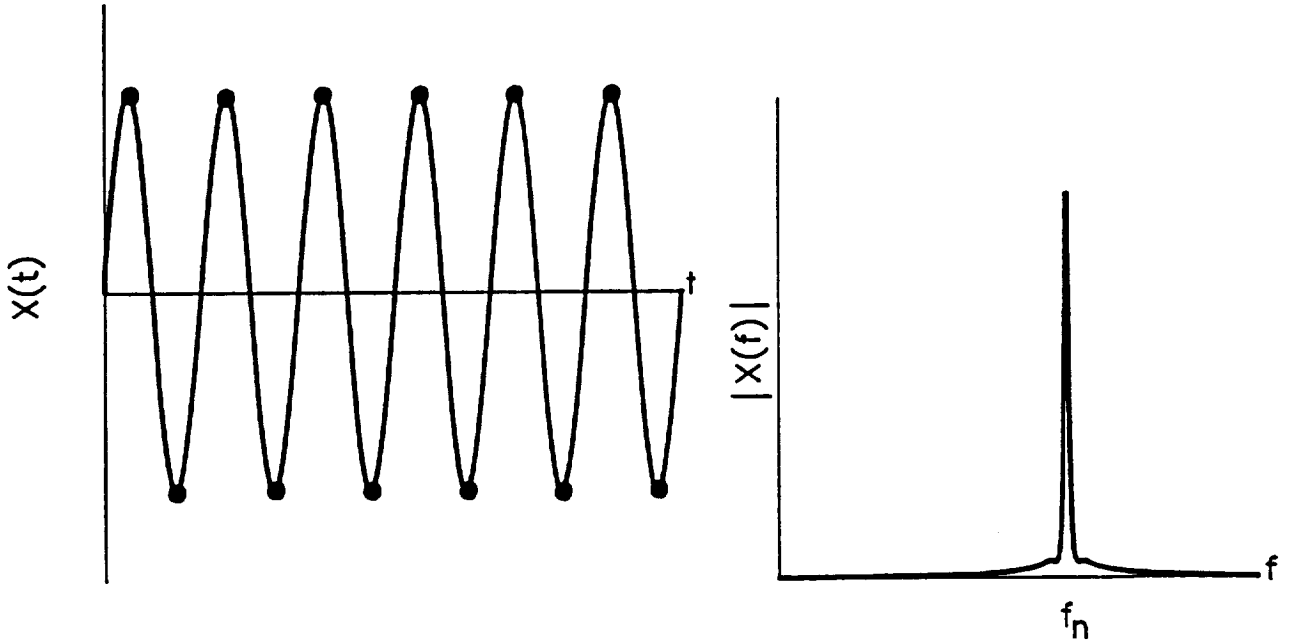

c) Ideal Sine Wave Sampled at a Sufficient Sampling Rate

d) FFT at a Sufficient Sampling Rate

Fig. A4 Aliasing of an Ideal Sine Wave

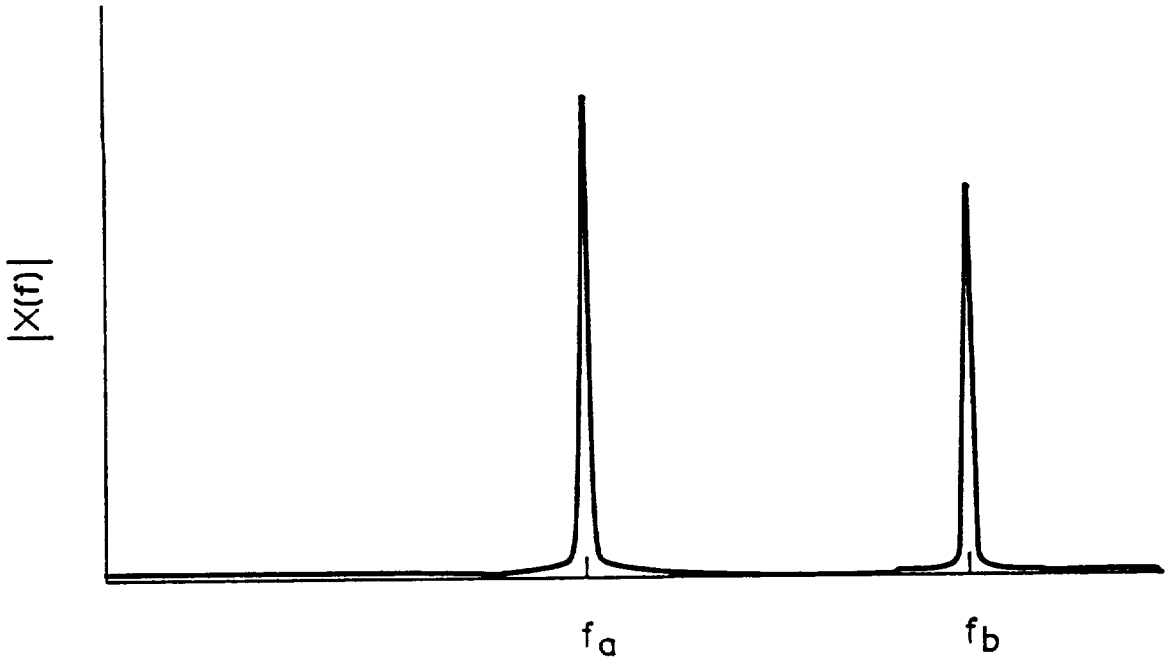

a) True Spectrum With a Signal Containing Two Frequency Components (f_a, f_b)

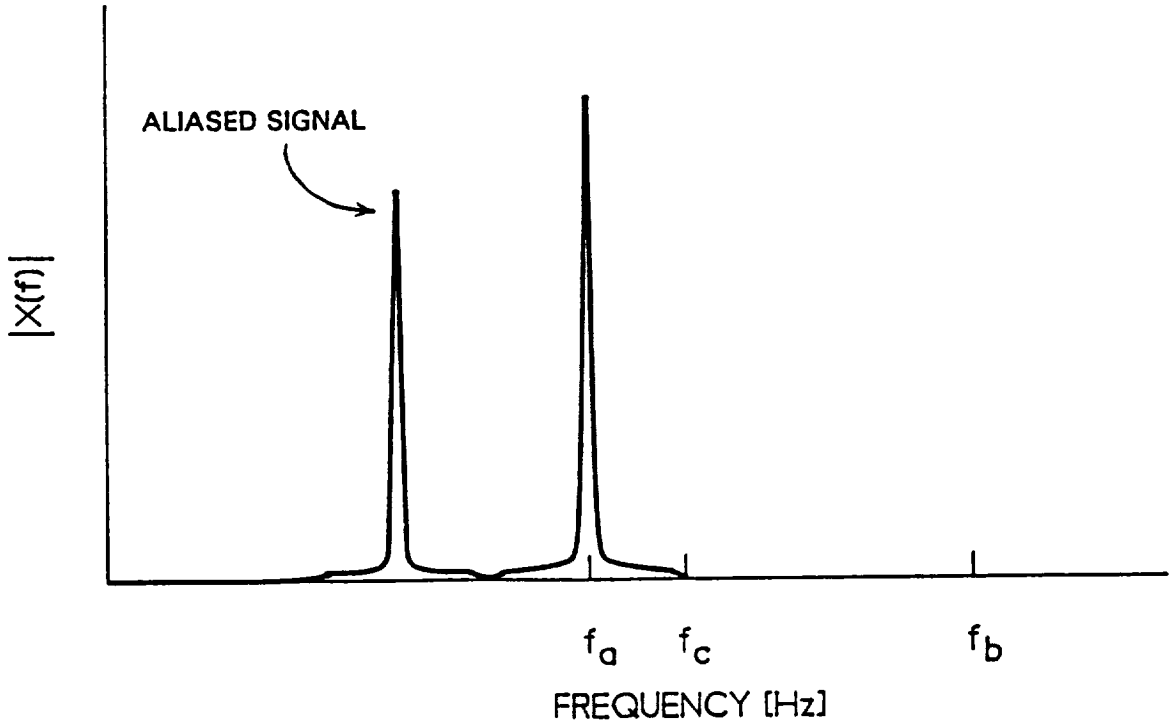

b) Observed Spectrum When Cutoff Frequency is Below f_b

Fig. A5 Aliasing when Multiple Frequencies are Involved

contains two frequency components, f_a and f_b. If this signal is sampled at a rate of $2f_c$, where $f_a < f_c < f_b$, the frequency, f_b, will be improperly detected or aliased because the sampling rate is too low (Fig. A5b).

In many cases the highest frequency in the data is unknown so physical means must also be used to minimize errors due to aliasing. Physical prevention of aliasing makes use of filters to remove high frequency signals and thereby establish a physical cutoff frequency (the cutoff frequency of the filter). Figure A6a illustrates a fictitious Fourier transform of a signal containing two groups of frequency components which lie reasonably close together. If the sampling rate of this signal corresponds to a cutoff frequency f_c, and a filter is not installed to eliminate high frequencies, aliasing will occur when the Fourier transform has been applied (Fig. A6b). The extent to which this problem can be corrected depends upon the attenuation characteristics of the physical filter through which the data are collected which are illustrated qualitatively in Fig. A6c. When an ideal filter with a cutoff frequency, f_c, is used to filter the signal (Fig. A6a) and the sampling rate is adequate ($>2f_c$), only frequencies below f_c are passed and the aliased portion is completely removed (Fig. A6d). With real filters, aliased signals are present to a lesser extent as the low and high attenuation filter curves in Fig. A6d suggest. Therefore, if a filter is used to eliminate frequency components above the frequency determined by the sampling rate, the effects of aliasing can be reduced to acceptable levels in the Fourier transform.

A summary of the appropriate steps which are taken to ensure an accurate FFT is illustrated in Fig. A7. First, a signal is passed through a low pass (or bandpass), high attenuation filter providing a physical cut-off frequency. Second, the data are sampled, or digitized, at a rate greater then or equal to twice the cut-off frequency to

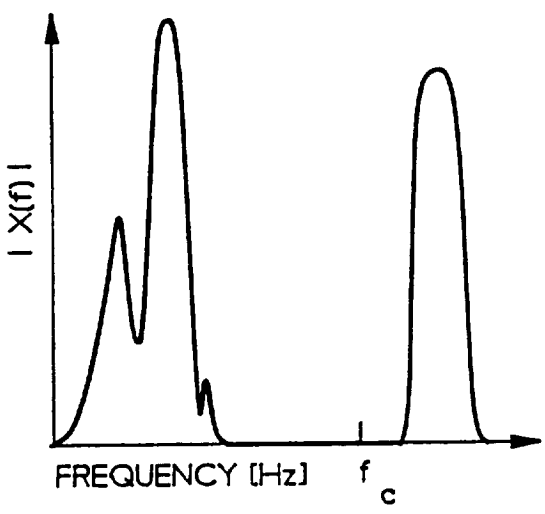

a) True Spectrum

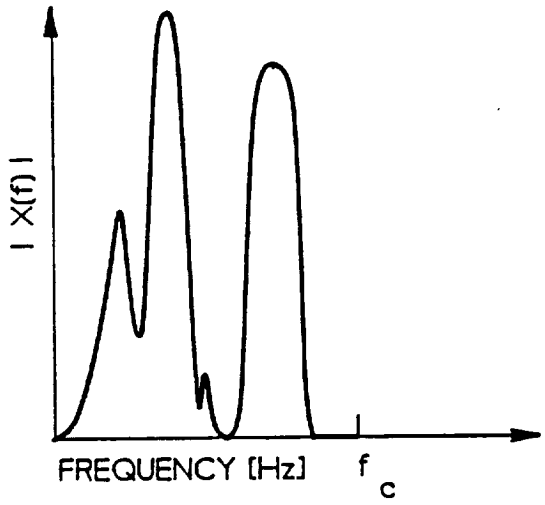

b) Aliased Spectrum

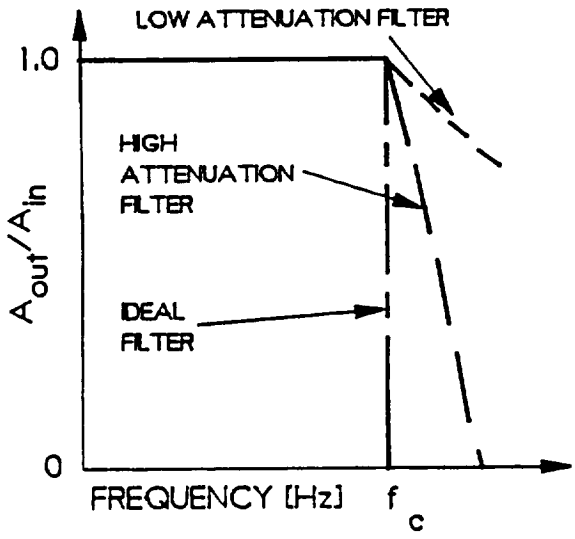

c) Filter Characteristics

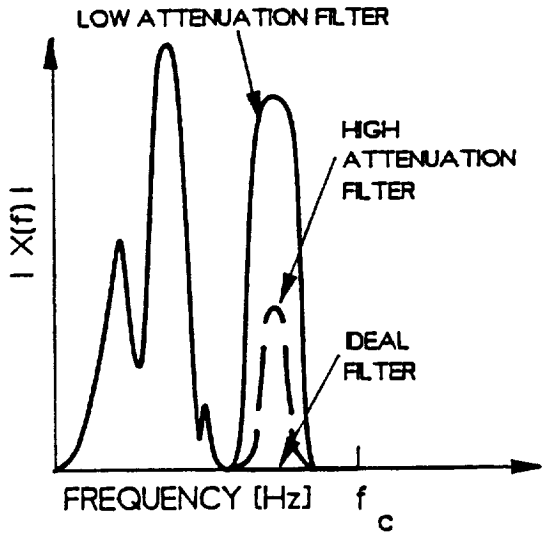

d) Filtered Spectrum

Fig. A6 Filter Effects on Aliasing

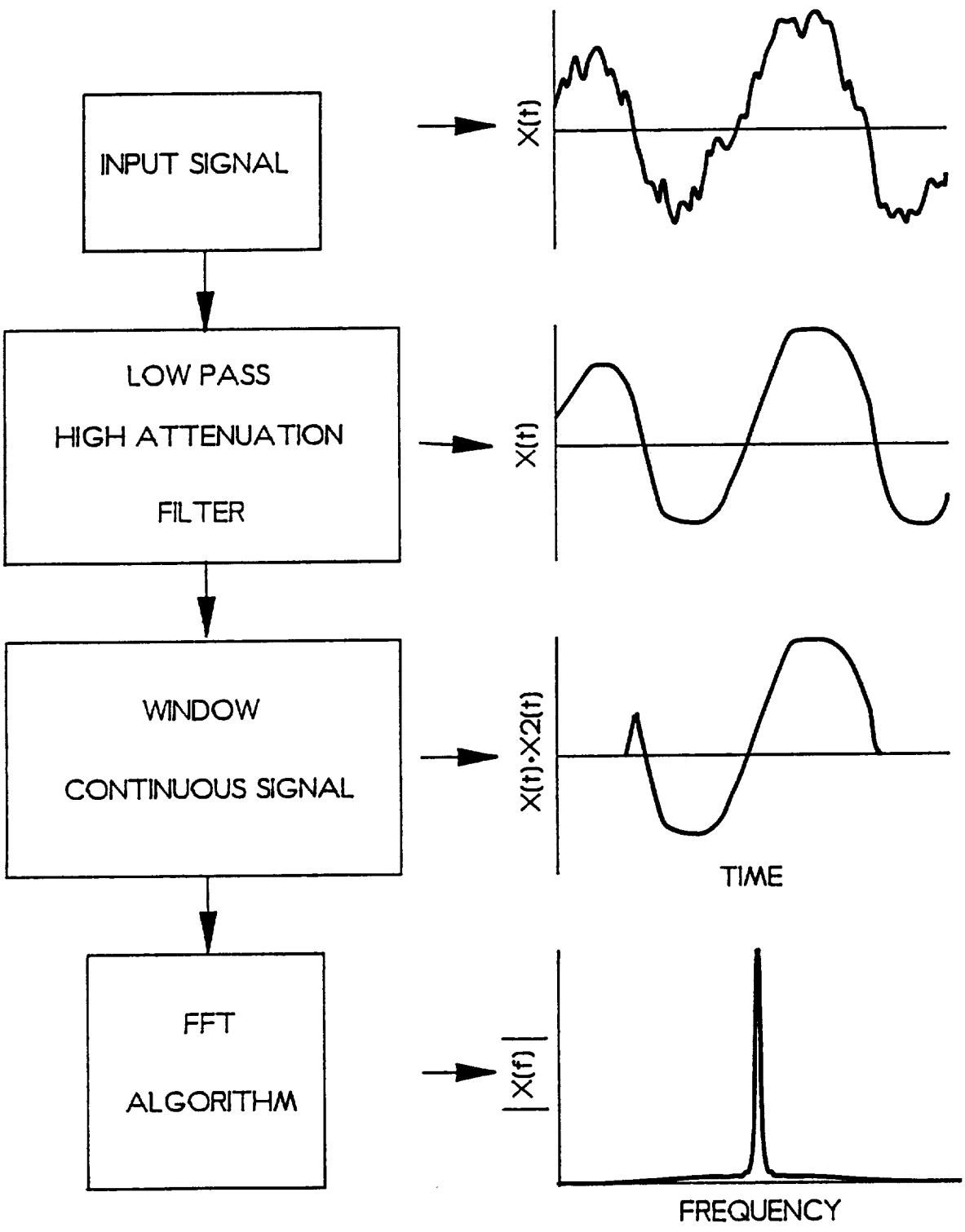

Fig. A7 Summary of Signal Processing Steps

prevent aliasing. Next, using a computer with the appropriate software, the digitized signal is windowed (a Hanning window is used for our analyses) and the fast Fourier transform is computed.

Interpreting Power Spectral Density Plots

After the FFT has been computed with acceptably small errors using the steps mentioned previously, results are often presented as autospectral, or power spectral, density plots (PSD). These plots are useful tools for studying noise because 1) dominant frequencies can be determined and 2) the rms value of a noise-related amplitude (e.g. current) over certain frequency ranges can be estimated. The PSD is defined as the mean-squared amplitude of a signal at a given frequency divided by the bandwidth associated with the measurement [9]. The bandwidth, which is the lowest frequency detectable by the FFT, is equal to 1/T where T is the window time. The PSD is estimated by squaring the amplitude corresponding to a particular frequency (computed from the FFT) and then dividing by this bandwidth. A typical PSD is plotted as a function of frequency in Fig. A8 where the scales are log-log and the units (for this case) are mean-squared current per unit bandwidth (mA^2/Hz). Power-spectral-density plots are frequently integrated over a prescribed frequency range to obtain a mean-squared value of the amplitude for that frequency range. For example, Fig. A9 shown the same PSD plot as Fig. A8 and illustrates the area between frequencies f_a and f_b is 900 mA^2. Therefore, the root-mean-square (rms) current for Fig. A9 in the frequency range 100 to 1000 Hz is 30 mA. The rms current for an entire PSD plot (Fig. 9, for example) is determined by integrating over the full frequency range (0 to ∞).

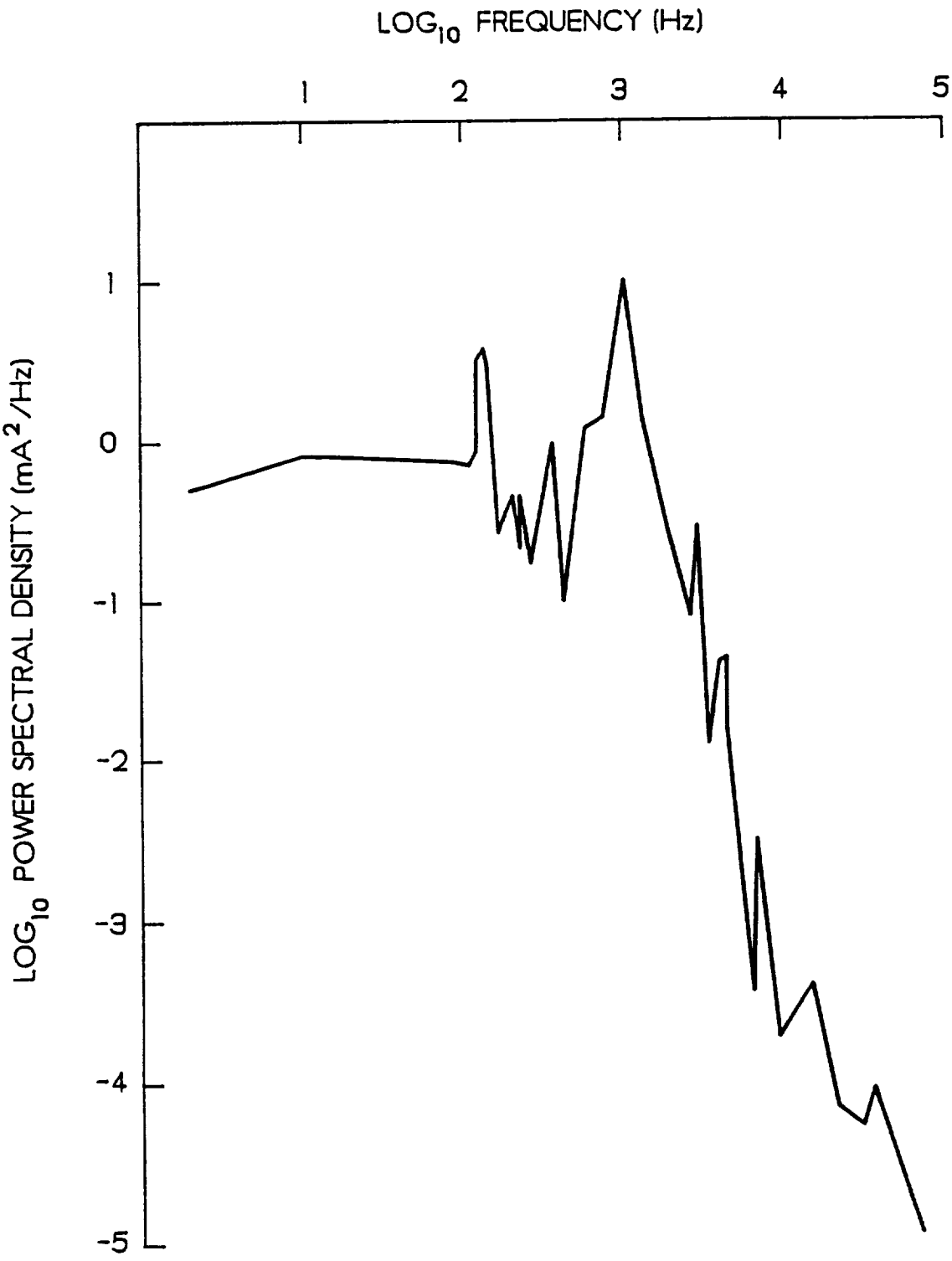

Fig. A8 Typical Power Spectral Density (PSD)

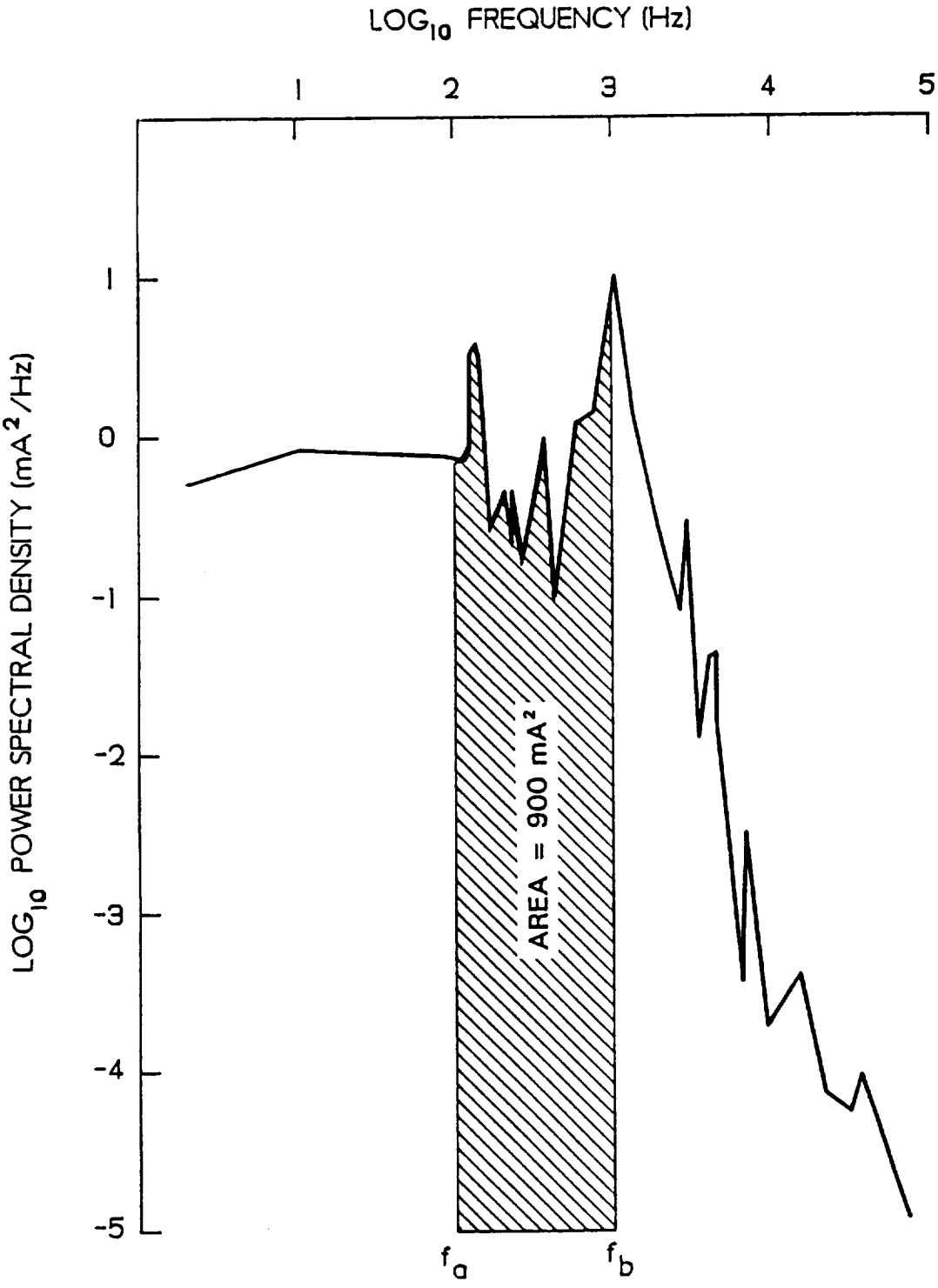

Fig. A9 Finding the RMS of a Band-pass Between Frequencies f_a and f_b

DISTRIBUTION LIST

	Copies
National Aeronautics and Space Administration Washington, DC 20546 Attn:	
Ms. Pat Conners, Code MD	1
Mr. Thomas D. Stuart, Code MK	1
Dr. Stanley Shawhan, Code ES	1
Dr. L.R. Owen Storey, Code ES	1
Mr. George Levine, Code MTF	1
Mr. Ivan Bekey, Code Z	1
Mr. John L. Anderson, Code RS	1
National Aeronautics and Space Administration Lewis Research Center 21000 Brookpark Road Cleveland, OH 44135 Attn:	
Technology Utilization Office, MS 7-3	1
Report Control Office, MS 60-1	1
Library, MS 60-3	2
Dr. M. Goldstein, Chief Scientist, MS 5-9	1
Mr. Dave Byers, MS 500-219	1
Mr. Vincent Rawlin, MS SPTD-1	1
Mr. Joseph C. Kolecki, MS 302-1	1
Mr. Michael Patterson, MS SPTD-1	1
Dr. Dale Ferguson, MS 302-1	1
Dr. Barry Hillard, MS 302-1	1
Dr. Willie Mackey, MS 302-1	1
Mr. Norman T. Grier, MS 302-1	1
Mr. Joel T. Galofaro, MS 302-1	10
National Aeronautics and Space Administration Lyndon B. Johnson Space Center Houston, TX 77058 Attn:	
Dr. James E. McCoy, Mail Code SN3	1
National Aeronautics and Space Administration Marshall Space Flight Center Huntsville, AL 35812 Attn:	
Mr. J. H. Laue, Mail Code FA31	1
Mr. Chris Rupp, Mail Code PS04	1
Mr. James K. Harrison, Mail Code PS04	1

	Copies
NASA Scientific and Technical Information Facility P.O. Box 8757 Baltimore, MD 21240 Attn: Accessioning Dept.	1
Dept. of the Navy Office of Naval Research University of New Mexico Bandolier Hall West Albuquerque, NM 87131 Attn: G. Max Irving	1
Procurement Executive, Ministry of Defense Royal Aircraft Establishment Farnborough, Hants GU14 6TD ENGLAND Attn: Dr. D. G. Fearn	1
United Kingdom Atomic Energy Authority Culham Laboratory Abingdon, Oxfordshire OX143DB ENGLAND Attn: Dr. A. R. Martin (Rm F4/135)	1
SRT Technologies 1500 Wilson Blvd, Suite 800 Arlington, VA 22209-2415 Attn: Ms. Kaye Anderson	1
Jet Propulsion Laboratory 4800 Oak Grove Laboratory Pasadena, CA 91109 Attn:	
Technical Library	1
Dr. John R. Brophy, Mail Code 125-224	1
Dr. Paul Penzo, Mail Code 1156-217	1
Dr. Stephen Gabriel	1

	Copies
TRW Inc. TRW Systems One Space Park Redondo Beach, CA 90278 Attn:	
Dr. Rob Stillwell	1
National Aeronautics and Space Administration Ames Research Center Moffett Field, CA 94035 Attn:	
Technical Library	1
National Aeronautics and Space Administration Langley Research Center Langley Field Station Hampton, VA 23365 Attn:	
Technical Library	1
Mr. Dick Deloach, Mail Code 234	1
Hughes Research Laboratories 3011 Malibu Canyon Road Malibu, CA 90265 Attn:	
Dr. Jay Hyman, MS RL 57	1
Dr. J. R. Beattie, MS RL 57	1
Dr. J. N. Matossian, MS RL 57	1
Dr. J. D. Williams, MS RL 57	1
Mr. Lee Parker 252 Lexington Road Concord, MA 01741	1
Department of Aeronautics and Astronautics Massachusetts Institute of Technology Cambridge, MA 02139 Attn:	
Dr. Daniel E. Hastings, Rm 37-441	1
Institute for Space and Aeronautical Science 4-6-1 Komaba, Meguro-ku, Tokyo, 153, JAPAN Attn:	
Prof. K. Kuriki	1
Prof. T. Obayashi	1

	Copies
Tokai University Kitakauame, Hiratsuka, Kanagawa, JAPAN Attn: Prof. K. Hirao	1
Physics Department Naval Postgraduate School Monterey, CA 93943-5000 Attn: Dr. Chris Olson, Mail Code 61-0S	1
Martin Marietta Aerospace P. O. Box 179 Denver, CO 80201 Attn: Dr. L. Kevin Rudolph, MS S8064	1
S-Cubed P. O. Box 1620 LaJolla, CA 92038 Attn: Dr. Ira Katz Dr. Victoria A. Davis	1 1
Electric Propulsion Laboratory, Inc. 440 N. Green St. Tehachapi, CA 93561 Attn: Dr. Graeme Aston	1
Mr. Joe Carroll Energy Science Laboratories, Inc. P.O. Box 85608 San Diego, CA 92138-5608	1
Science Applications International Corp. 13400 B Northrop Way #36 Bellevue, WA 98005 Attn: Dr. Hugh Anderson	1

	Copies
Istituto di Fisica dello Spazio Interplanetario Consiglio Nazionale delle Ricerche Via G. Galilei 00044 Frascati, ITALY Attn:	
Dr. Marino Dobrowolny	1
Dr. Carlo Bonifazi	1
Dr. Luciano Iess	1
Dr. Giuliano Vannaroni	1
Starlab/SEL Stanford University Stanford, CA 94305 Attn:	
Dr. Peter Banks	1
Dr. Roger Williamson	1
Science Applications International Corp. Plasma Physics Division 1710 Goodridge Drive McLean, VA 22102 Attn:	
Mr. Edward P. Szuszczewicz	1
University of Alabama (Huntsville) Electrical and Computer Engineering Dept. Engineering Building Huntsville, AL 35899 Attn:	
Dr. Michael Greene	1
Physics Department Utah State University Logan, Utah 84322 Attn:	
Dr. W.J. Raitt	1
Grumman Corp. 420 Wynn Dr. Huntsville, AL 35805 Attn:	
Dr. Kai-Shen Hwang	1

	Copies
Dr. Roy Torbert Space Science Center Rm. 406 University of New Hampshire Durham, NH 03824	1
Institut f. Geophysik u. Meteorology Albertus-Magnus-Platz D-5000 Köln 41 West Germany Attn: Mr. Hartmut Marschall	1
Capt. Lon Enloe GL(AFSC)/PHP Hanscom AFB, MA 01731-5000	1
W. J. Schafer Assoc. Inc. 1901 North Fort Meyer Dr., Suite No. 800 Arlington, VA 22209 Attn: Dr. Herbert Cohen	1